CAMBRIDGE
UNIVERSITY PRESS

Article

Mineralogy of the scheelite-bearing ores of Monte Tamara, SW Sardinia: insights for the evolution of a Late Variscan W–Sn skarn system

Matteo L. Deidda[1]* , Stefano Naitza[1] , Marilena Moroni[2], Giovanni B. De Giudici[1] , Dario Fancello[1] , Alfredo Idini[1] and Andrea Risplendente[2]

[1]Dipartimento di Scienze Chimiche e Geologiche, Università degli Studi di Cagliari, Cittadella Universitaria, Blocco A, 09042 Monserrato CA, Italy; and [2]Dipartimento di Scienze della Terra, Università degli Studi di Milano, Via Luigi Mangiagalli, 34, 20133 Milano MI, Italy

Abstract

Southwestern Sardinia, Italy, hosts several skarn, W–Sn–Mo greisen and hydrothermal deposits related to a 289±1 Ma Late Variscan granite suite. Among them, the most representative scheelite-bearing skarns belong to the San Pietro and Sinibidraxiu localities, in the Monte Tamara area, Sulcis region. The San Pietro deposit is a typical calc-silicate skarn whereas Sinibidraxiu is a sharply bounded orebody hosted in a marble unit. Optical petrographic observations and compositional data of major and trace elements were obtained for samples from both localities. San Pietro data suggests evolution from an oxidising prograde skarn stage (andradite–diopside, hematite and scheelite), to progressively more reducing conditions from the early retrograde (magnetite–cassiterite) to the late sulfide stage (arsenopyrite, stannite, molybdenite, Bi sulfosalts and Zn–Cu–Pb–Fe sulfides); Sinibidraxiu has diffuse carbonate–quartz intergrowths pseudomorphic over an early mineral assemblage with fibrous habit, followed by abundant ore mineral precipitation under reducing conditions (scheelite, arsenopyrite and Pb–Zn–Cu–Fe sulfides). Geothermometers indicate a comprehensive temperature range of 460–270°C for the sulfide stages of both deposits. The differences between the two deposits might be controlled by the distance from the source intrusion coupled with the different reactivity of the host rocks. The San Pietro mineralogy represents a more proximal skarn, contrasting with more distal mineralogical and chemical features characterising the Sinibidraxiu orebody (lack of Mo–Sn–Bi phases; LREE–MREE–HREE signature of scheelite). This investigation contributes for the first time to the identification of a W–Sn skarn system in SW Sardinia, thereby suggesting the Monte Tamara area and its surroundings as favourable for further exploration.

Introduction

Skarns are a common class of ore deposits and are generally classified into seven major types of economic significance on the basis of the dominant economic metal (Fe, Au, Cu, Zn, W, Sn, Mo skarns; Einaudi *et al.*, 1981; Meinert *et al.*, 2005). In each major skarn type, their particular ore mineral associations, relative abundances and mineral composition are strongly dependent on the metallogenic features of the parental intrusions (Meinert *et al.*, 2005; Chang *et al.*, 2019). Skarn deposits are typically regarded as relevant sources of strategic and critical elements (Meinert *et al.*, 2005; Chang *et al.*, 2019; US Geological Survey, 2021). This has triggered new interest in these deposits in different European districts in which the historical mining areas host

numerous, poorly exploited and/or underexplored skarns; among them, W- and Sn-bearing skarns, which are typically poorly constrained in many Variscan regions of Europe (Burisch *et al.*, 2019). In the ore districts of SW Sardinia, W-bearing skarns hosted in the Palaeozoic basement and related to Late Variscan granitoids are mentioned only in older literature (Valera And Zuffardi, 1968, 1970; Valera, 1970; Venerandi Pirri, 1971; Verkaeren and Bartholomé, 1979; Aponte *et al.*, 1988), where scheelite was reported as an accessory mineral in association with Pb–Zn–Cu sulfide and Fe-oxide ores. Moreover, numerous old mine reports indicate only small amounts of scheelite in ore and in dressing plant concentrates, and the presence of cassiterite in the skarn ores is noted repeatedly in reports by mineral collectors (Brizzi *et al.*, 1992a, 1992b; Olmi *et al.*, 1995).

New research themes for critical raw materials in Sardinia (Naitza *et al.*, 2019) have revitalised interest in a broad re-examination of already known skarn-related deposits and mineral occurrences. Similarly, investigations of a Late Variscan

F-bearing, ilmenite-series (Ishihara, 1981) ferroan granite suite, exposed extensively in SW Sardinia (GS1 suite: Conte *et al.*, 2017) and accompanied by Sn–W–Mo mineralisation, confirmed the metallogenic potential of this setting (Naitza *et al.*, 2015; Naitza *et al.*, 2017). The area of Monte Tamara, located in the southern part of SW Sardinia (Sulcis region), displays some of the most interesting and least known occurrences of W- and Sn-bearing Pb–Zn–Cu sulfide and Fe-oxide skarns, related spatially and possibly genetically to GS1 suite ferroan granites. This investigation provides the first detailed characterisation of the main occurrences of the Monte Tamara area and their different mineral parageneses, with the objective of better understanding the formation processes of the mineralisation, defining the spatial evolution of the skarn system and obtaining useful indications for W and Sn exploration in the Sardinian Variscan districts.

Geological setting

The Monte Tamara area is located in the Sulcis region, the SW edge of Sardinia, which represents a foreland area in the Southern Variscan chain (Rossi *et al.*, 2009). In the Sulcis region, two main Palaeozoic deformations occurred: (1) an initial kilometre-scale E–W trending syncline–anticline fold system related to the Early–Middle Ordovician 'Sardic Phase' (Cocco *et al.*, 2018, 2022b, and references therein); (2) a Variscan multi-stage folding, resulting in amplification of the previous E–W structures followed by N–S and NNE–SSW-trending folds (Arthaud, 1963; Poll and Zwart, 1964; Funedda, 2009). The Variscan structures affect two main very low-grade sedimentary mega-sequences separated by an angular unconformity ('Sardic unconformity'; Stille, 1939). The first Early Cambrian–Early Ordovician mega-sequence (Cocozza, 1979) includes two siliciclastic units (Nebida Formation and Cabitza Formation), a thick carbonate unit (Gonnesa Formation), and a thin nodular silty limestone unit (Campo Pisano Formation). The Gonnesa Formation is the host of the large MVT Pb–Zn sulfide deposits of the Iglesiente–Sulcis district (Boni *et al.*, 1996). The second mega-sequence is a thick Middle–Late Ordovician siliciclastic sequence (Leone *et al.*, 1991), capped by Silurian–Early Devonian carbonaceous black shales and limestones.

The Monte Tamara area is located in the Early Cambrian–Early Ordovician pre-Variscan low-grade metasedimentary sequence, arranged in a large N–S anticline–syncline fold system related to the Variscan stage (Fig. 1). From the bottom to the top, the folding system includes meta-sandstones of the Nebida Formation (early Cambrian) overlapped by carbonate rocks of
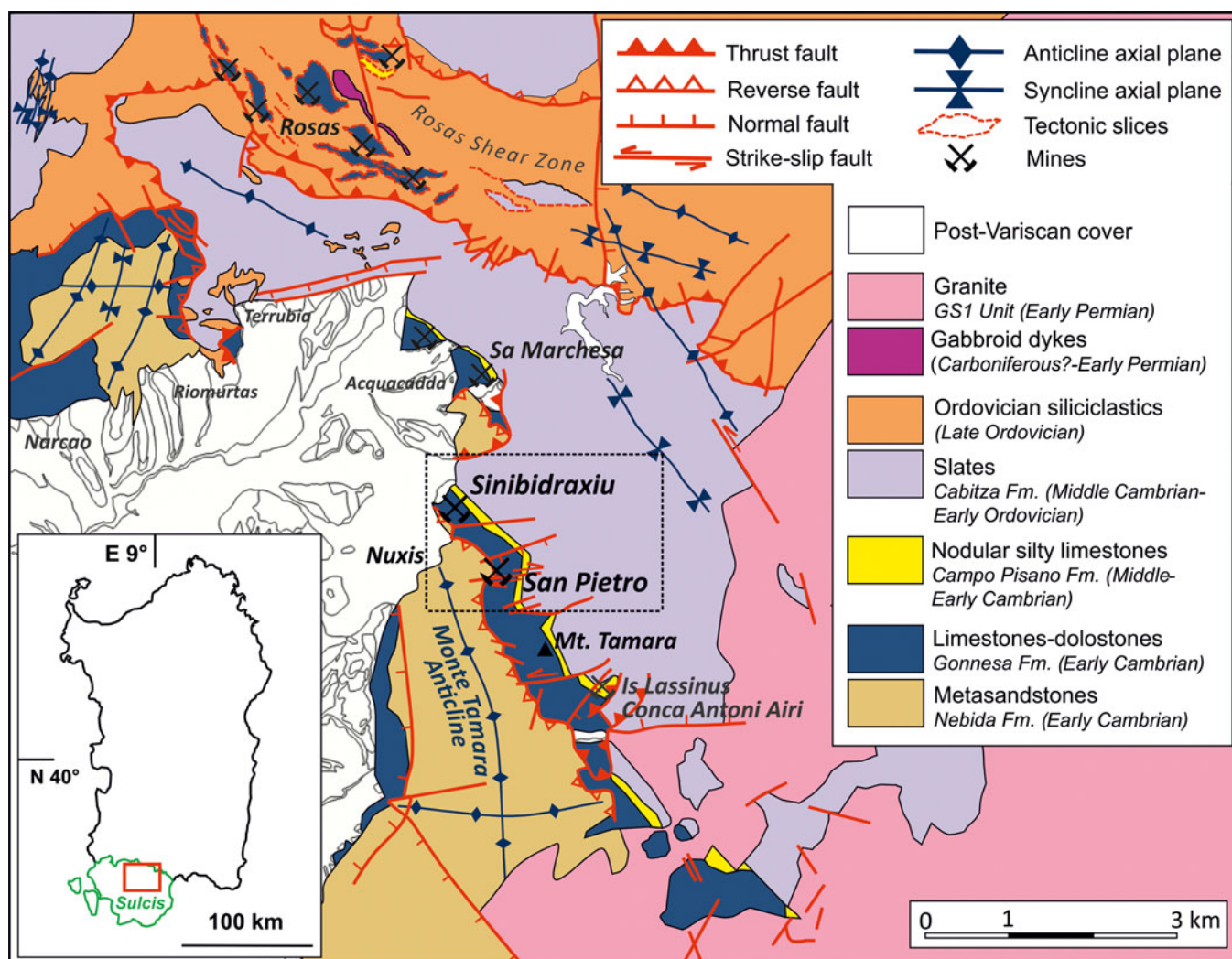

Fig. 1. Simplified geological map of the Monte Tamara area, SW Sardinia; the San Pietro and Sinibidraxiu abandoned mines are highlighted by the black rectangle.

the Gonnesa Formation (early Cambrian), nodular silty limestones of the Campo Pisano Fm (middle–early Cambrian) and slates from the Cabitza Formation (middle Cambrian–early Ordovician). Tectonic contacts between these formations are produced by low-angle NNW–SSE striking reverse faults and later steeply dipping NE–SW striking normal faults (Barca et al., 2009). During Late Variscan post-collisional stages the Sulcis region, including the Monte Tamara area, was intruded by a granite suite ('GS1 suite', Conte et al., 2017). The GS1 suite consists of F-bearing, ferroan (FeO/[FeO + MgO]>0.90) ilmenite series, slightly peraluminous monzogranites and leucogranites (Conte et al., 2017). Relevant accessory minerals are ilmenite, xenotime-Y and fluorite. Intrusive bodies are affected locally by alkaline metasomatism and greisenisation with associated Mo–W–Sn mineralisation (Naitza et al., 2017). The suite was emplaced at shallow crustal levels (~1 kbar; Conte et al., 2017) in the Early Permian (289±1 Ma by Re–Os on molybdenite; Boni et al., 2003), forming extended low-angle-dipping bodies under the metasedimentary formations (Naitza et al., 2017). As a result, evidence for contact-metamorphism (spotted schists, marbles, skarns and hornfelses on the Nebida, Gonnesa-Campo Pisano and Cabitza Formations) and skarn mineralisation is common. Skarn deposits in this region are located typically along pre-existing Variscan structures and tectonic contacts between carbonate and siliciclastic units. These structural relationships are particularly evident in the neighbouring, highly-deformed Rosas mine area, where numerous mineralised skarns occur in limestone–dolostone tectonic slices throughout the Ordovician siliciclastic sequence (Cocco et al., 2022a; Funedda, 2009).

The San Pietro and Sinibidraxiu orebodies

The Monte Tamara area hosts numerous mineworkings among which the most important were the San Pietro and Sinibidraxiu historic mines. These have been active since the late 19th Century until the second half of the 20th Century and exploited Zn–Pb–Cu–As ores. Although the presence of scheelite was known (Valera and Zuffardi, 1968, 1970; Valera, 1970) its occurrence remained uncharacterised and both deposits have been described generically as skarn-type (Salvadori and Zuffardi, 1961). However, despite many similarities, the San Pietro and Sinibidraxiu orebodies exhibit significant differences in terms of geometry, texture, gangue and mineral assemblages.

The San Pietro mine (Fig. 1) consisted of five underground mining levels through a vertical depth of ~70 m (Fig. 2a). The mine exploited a 0.5–5 m thick and irregular, steeply dipping band of dark green skarn (Fig. 3a) located between the meta-sandstones (Nebida Formation) and greyish black marbles (Gonnesa Formation) with disseminated Zn–Pb–Cu sulfides and narrow subvertical veins. Well-exposed mineralised skarn outcrops are limited to an open excavation and a stope close to a shaft at the top of the mine (level 377 in Fig. 2a). The ore is a 5 m thick, NW–SE striking and steeply SW-dipping band, consisting of four main zones (1–4 in Fig. 3a). From the meta-sandstones to the marbles: the first zone (1) is a 50 cm thick garnet–clinopyroxene–wollastonite skarn band with magnetite, chalcopyrite and scheelite; followed by (2) a zone of 30 cm thick magnetite and sphalerite band in a garnet and amphibole gangue; (3) the magnetite band grades towards an arsenopyrite–sphalerite–chalcopyrite–galena zone; and (4) towards the contact with the marbles, a 30 cm thick band of massive magnetite hosts

subordinate chalcopyrite and mm-scale dispersed crystals of scheelite (observed under short-wave UV light) in an amphibole gangue. Due to the inaccessibility of underground mineworks and to the scarcity of skarn outcrops, hand specimens from the lower parts of the orebody (Fig. 2a) were collected from small ore stockpiles in front of the main adits. They include medium- to coarse-grained dark green garnet, clinopyroxene and wollastonite rocks with magnetite and chalcopyrite cross-cutting veinlets and disseminations of millimetric crystals of scheelite. Chalcopyrite, galena and sphalerite are commonly found as space-filling veins and grains in garnet–clinopyroxene specimens, and in retrograde amphibole- and epidote-rich facies. Specimens from the massive sulfide veins include fine- to medium-grained aggregates of chalcopyrite, sphalerite, arsenopyrite, galena and pyrite, commonly intergrown with magnetite. Secondary Fe-Cu–Zn–As minerals are common and renowned among mineralogists and mineral collectors (https://www.mindat.org/loc-56421.html: San Pietro Mine, Tamara Mountain, Nuxis, South Sardinia Province, Sardinia, Italy).

The Sinibidraxiu mine is located on the NW edge of the Monte Tamara ridge, ~2 km north of the San Pietro mine (Fig. 1). The mine can be accessed underground by an E–W stope of 200 m in length, excavated primarily in the Cambrian carbonate rocks of the Gonnesa Formation (Fig. 2b). The thermal recrystallisation increases eastwards, and limestone–dolostone grade into marbles with sporadic disseminations of Zn–Pb sulfides. In the main orebody is a 1 m thick and 4 m large, vertical and flattened chimney hosted in dolomitic marbles. This is located at the intersection between two NNE–SSW and ESE–WSW striking fractures (Fig. 2b), and extends for ~60 m upwards to the surface, where it presents as a small gossan deposit. In the underground exposure, five zones (1–5 in Fig. 3b) can be recognised. Zone 1 is a 30 cm thick arsenopyrite + scheelite + Ca–Mg-carbonates association. Arsenopyrite is the most abundant mineral occurring as lustrous grey, idiomorphic and centimetre-sized crystals, intergrown with carbonates and milky-white idiomorphic scheelite crystals. Scheelite ranges from few mm to 2 cm in size and can be distinguished from carbonates under short-wave ultraviolet light. In the 20 cm thick-zone 2, arsenopyrite, carbonates and quartz are the most abundant minerals, with subordinate scheelite and sphalerite. Arsenopyrite, less abundant than in zone 1, is enclosed in a pale greenish carbonates and quartz matrix forming large radiate/fibrous aggregates. Scheelite here occurs as millimetre- to centimetre-sized grains, scattered irregularly inside the carbonates–quartz aggregates. Arsenopyrite decreases gradually towards zone 3 in favour of a sphalerite ± scheelite association in the carbonates–quartz matrix, here assuming a brownish-green colour and forming larger radiate aggregates (2 cm in diameter). Centimetre-sized grains of dark sphalerite are observed at the core of the aggregates, resembling cockade-type textures. Scheelite disseminations within these cockades become more sporadic. Zone 4 is an arsenopyrite + calcite veinlet marking the contact between the ore and marbles. Lastly, irregular veinlets and pockets of massive sulfides of zone 5, consisting of sphalerite, arsenopyrite, chalcopyrite, galena and pyrite associated with calcite–dolomite and baryte, crosscut the other associations. The macroscopic features of the ores in representative samples are shown in Fig. 4.

Materials and methods

Two main sites of the Monte Tamara area have been surveyed and sampled in this study: the San Pietro mine and the Sinibidraxiu
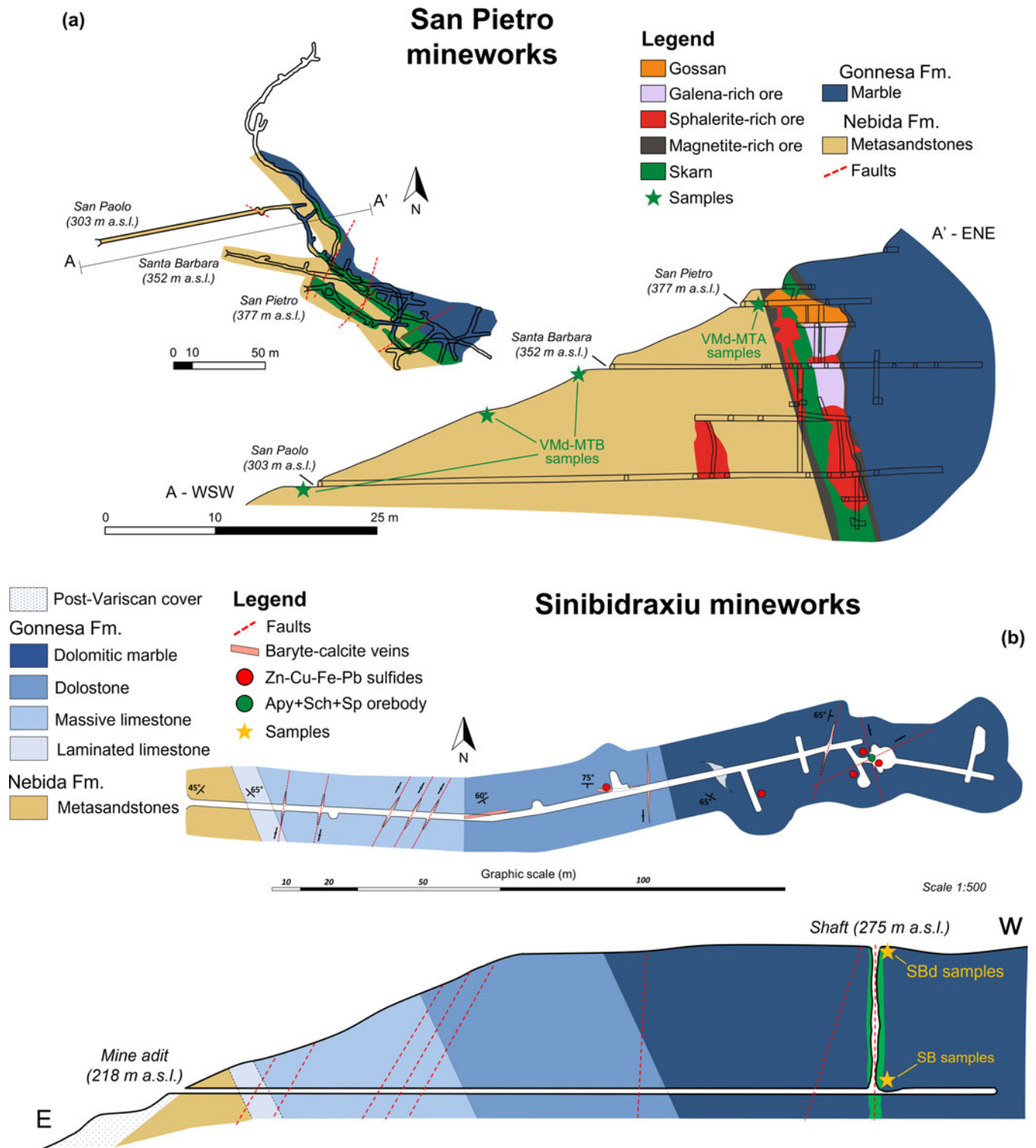
Fig. 2. Geological sketches and cross-sections of the San Pietro (a) and Sinibidraxiu (b) mines with sampling points indicated in the cross-sections. At San Pietro, VMd samples were collected from mine dumps across all levels of the mine; MTB and MTA samples belong to the lower and upper levels respectively. At Sinibidraxiu, SB samples were collected from the outcrops at the lower level of the mine; SBd samples were collected from the mine dumps at the upper level. In (a) the plant and the projection of the mineworks in the A–A' cross-section have been modified after Salvadori and Zuffardi (1961) and old mine maps, respectively. Mineral abbreviations (Warr, 2021): Apy = arsenopyrite; Sch = scheelite; Sp = sphalerite.

mine. Broad sampling from skarn and wall-rock outcrops, mine dumps and from the ores exposed in underground stopes was carried out. In each locality, preliminary evaluation for the presence of scheelite in the exposed ores was performed with a short-wave ultraviolet-light torch. After field observations (Fig. 3), a selection of more than a hundred samples was made on the basis of their macroscopical features of mineralisation and texture (Fig. 4, Supplementary table S0). After the sampling, 23 thin sections,
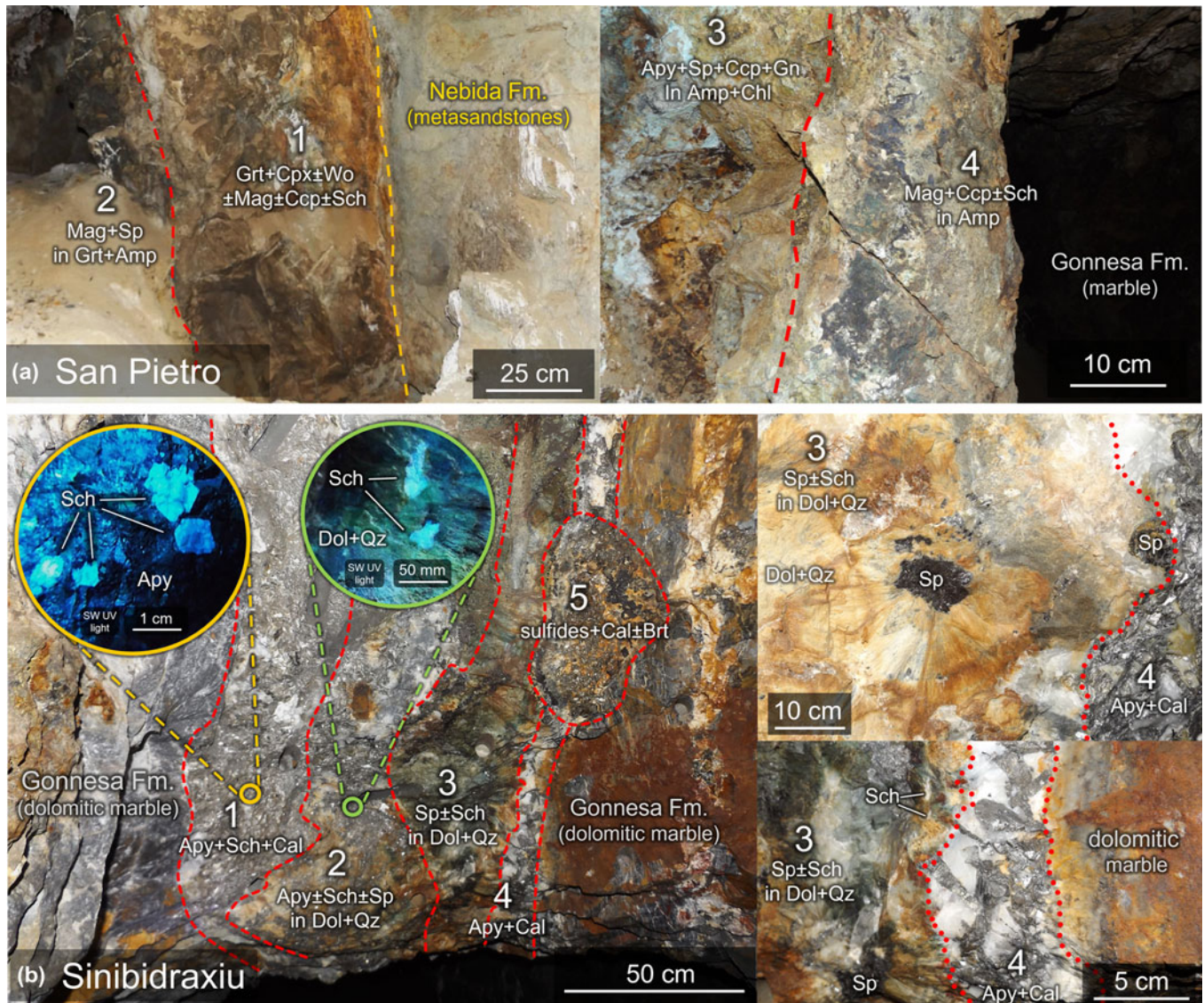
Fig. 3. Macroscopic zonation of the orebodies based on the occurrence of the major phases. At San Pietro (a), four main assemblages can be recognised and consist of: (1) magnetite + chalcopyrite ± scheelite in a garnet + clinopyroxene ± wollastonite gangue; (2) magnetite + sphalerite in a garnet + amphibole gangue; (3) arsenopyrite + sphalerite + chalcopyrite + galena in an amphibole + chlorite gangue; (4) magnetite + chalcopyrite ± scheelite in amphibole gangue. At Sinibidraxiu, five zones have been recognised: (1) arsenopyrite + scheelite and calcite; (2) arsenopyrite ± scheelite ± sphalerite in a dolomite–quartz gangue; (3) sphalerite ± scheelite in a dolomite–quartz gangue; (4) arsenopyrite and calcite; (5) sulfides (arsenopyrite, sphalerite, chalcopyrite, galena) in a calcite–baryte gangue. For each zone of the two deposits, the corresponding thin sections, polished mounts and polished slabs are reported in Supplementary Tables. Mineral abbreviations (Warr, 2021): Grt = garnet; Cpx = clinopyroxene; Wo = wollastonite; Amp = amphibole; Chl = chlorite; Mag = magnetite; Sch = scheelite; Apy = arsenopyrite; Sp = sphalerite; Ccp = chalcopyrite; Gn = galena; Cal = calcite; Dol = dolomite; Qz = quartz, Brt = baryte.

three polished slabs and 20 polished mounts were made from San Pietro (labelled VMd, MTB and MTA); six thin sections and 15 polished mounts were made from Sinibidraxiu (labelled SB and SBd). Thin sections and polished rock chips were investigated by optical microscopy in transmitted and reflected light and selected samples underwent scanning electron microscopy (SEM) analyses at CESAR laboratories of Università di Cagliari, using a Quanta FEI 200 unit equipped with a Thermo Fischer Ultradry EDS detector under low-vacuum conditions, 25–30 KeV voltage and 0.3–0.5 torr variable pressure. Quantitative wavelength dispersion spectrometry (WDS) microanalyses of sulfides, oxides and silicates were performed by means of a JEOL JXA–8200 electron probe equipped with five wavelength-dispersive spectrometers at the Dipartimento di

Scienze della Terra, Università Statale di Milano. The elements analysed with standards (pure metal or mineral), analytical/spectral lines, monochromators and detection limits in brackets are: Zn (Zn, $K\alpha$, LIFH, 650); Fe (fayalite, $K\alpha$, LIFH, 330); Cd (Cd, $L\alpha$, PET, 280); Cu (Cu, $K\alpha$, LIFH, 550); Ag (Ag, $L\alpha$, PET, 260); Ni (nickeline, $K\alpha$, LIFH, 350); Co (Co, $K\alpha$, LIFH, 350); Ge (Ge, $L\alpha$, TAP, 230); In (In, $L\alpha$, TAP, 600); Mn (rhodonite, $K\alpha$, LIFH, 350); Pb (galena, $M\alpha$, PET, 450); Sn (Sn, $L\alpha$, TAP, 350); Bi (Bi, $M\alpha$, PET, 330); Sb (Sb, $L\alpha$, TAP, 450); As (nickeline, $L\alpha$, TAP, 200); Te (Te, $L\alpha$, TAP, 500); S (pyrite, $K\alpha$, PET, 100); Se (HgSe, $K\alpha$, LIFH, 200); Ca (grossular, $K\alpha$, PETH, 140); Si and Al (grossular, $K\alpha$, TAP, 200 and 140); Na (omphacite, $K\alpha$, TAP, 240); K (K-feldspar, $K\alpha$, PETH, 170); Mg (olivine, $K\alpha$, TAP, 200); Ti (ilmenite, $K\alpha$, PETJ, 220); Cr (Cr, $K\alpha$, PETJ, 400); V
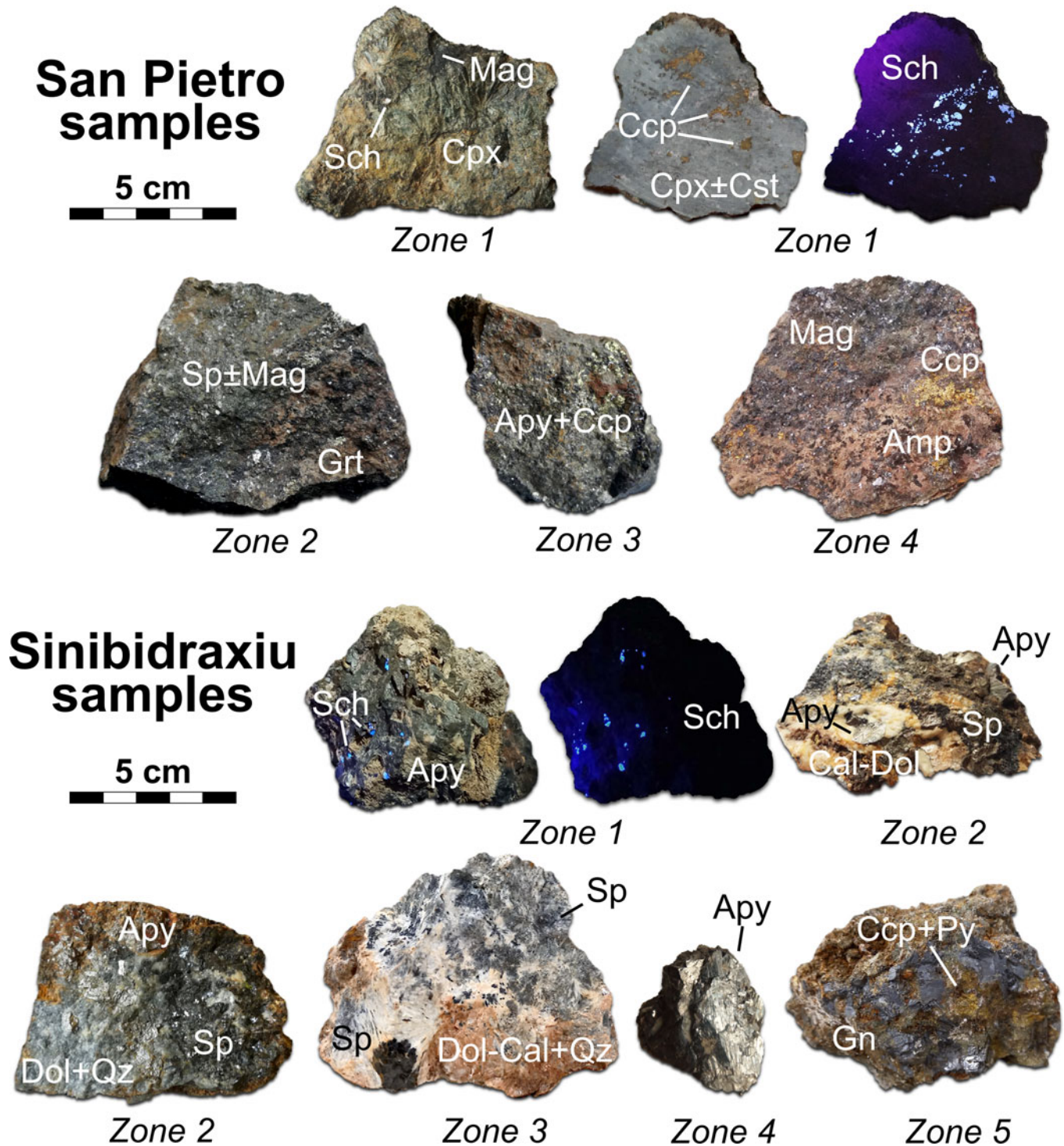
Fig. 4. Representative specimens from each zone of the San Pietro and Sinibidraxiu orebodies from which the samples indicated in Supplementary Tables have been selected. Mineral abbreviations (Warr, 2021): Grt = garnet, Cpx = clinopyroxene; Amp = amphibole; Chl = chlorite; Mag = magnetite; Sch = scheelite; Apy = arsenopyrite; Sp = sphalerite; Ccp = chalcopyrite; Gn = galena; Py = pyrite; Cal = calcite; Dol = dolomite; Qz = quartz; Brt = baryte.

(V, $K\alpha$, LIFH, 350); and W (W, $L\alpha$, LIFH, 2000). The analytical conditions for the electron beam were: accelerating voltage = 15 kV, beam current = 5 nA, beam diameter = 1–2 μm, counting time of 30 s on peak and 10 s on background for each element. Elemental concentrations were determined after applying the $\varphi(\rho z)$ algorithm and corrections for X-ray fluorescence, absorption, atomic number (Z) and matrices, and by evaluating spectral interferences. Analyses were performed after verifying that I_{xstd}/I_{std} was 1.00 ± 0.01 for each element, where I_{xstd} was the intensity of the analysed standard and I_{std} the intensity of the same standard checked after calibration for each element. Quantitative, *in situ* trace-element analysis of scheelite crystals from Monte Tamara and Sinibidraxiu were performed by means of an inductively coupled mass spectrometer Thermo Fisher Scientific iCAP

RQ quadrupole coupled with a Teledyne Cetac Technologies Analyte Excite 193 nm excimer laser, equipped with a HelEx 2 volume sample cell. These instruments are located at the LASA laboratories, Earth Science Department, State University of Milano. Diameters of laser spots were of 40 μm. The repetition rate was of 10 Hz with a fluence of 2 J/cm². The analytical routine included the acquisition of a background signal for 40 s, then analysis with laser ablation for 60 s, followed by 20 s of line purification. The NIST612 glass was used as the primary standard and the BCR–2g glass as a secondary standard. The Ca content determined by microprobe analysis was used as the internal standard for correcting the differences in performance in the ablation between the glass standards and the minerals. The software *Glitter* (Griffin *et al.*, 2008) was employed for the revision of the signals from the spectrometer, the recalculation and the data elaboration. The following elemental isotopes were analysed: ^{7}Li, ^{9}Be, ^{11}B, ^{25}Mg, ^{29}Si, ^{31}P, ^{43}Ca, ^{44}Ca, ^{45}Sc, ^{49}Ti, ^{51}V, ^{53}Cr, ^{55}Mn, ^{59}Co, ^{60}Ni, ^{Cu}65, ^{66}Zn, ^{69}Ga, ^{73}Ge, ^{75}As, ^{77}Se, ^{85}Rb, ^{88}Sr, ^{89}Y, ^{90}Zr, ^{93}Nb, ^{95}Mo, ^{111}Cd, ^{113}In, ^{115}In, ^{118}Sn, ^{121}Sb, ^{133}Cs, ^{137}Ba, ^{139}La, ^{140}Ce, ^{141}Pr, ^{146}Nd, ^{149}Sm, ^{151}Eu, ^{157}Gd, ^{159}Tb, ^{163}Dy, ^{165}Ho, ^{167}Er, ^{169}Tm, ^{173}Yb, ^{175}Lu, ^{177}Hf, ^{181}Ta, ^{182}W, ^{205}Tl, ^{208}Pb, ^{209}Bi, ^{232}Th and ^{238}U. Precision was better than 5% for rare earth elements (REE), large ion lithophiles and high-field-strength elements and better than 10% for other elements. Accuracy was within 2σ of the preferred values. Mineral abbreviations throughout the text are used according to Warr (2021). The compositional data are shown in detail in Tables S1–14 in the Supplementary materials.

Mineral associations and micro-textures

The San Pietro orebody features a wide variety of gangue, ore minerals and micro-textures. Samples from zone 1 (Figs 3a–4) minerals and micro-textures. Samples from zone 1 (Figs 3a–4)

of San Pietro include garnet, clinopyroxene, wollastonite, hematite, magnetite, scheelite, chalcopyrite, chlorite, amphibole, epidote, cassiterite, native Bi, bismuthinite, Bi–Pb–Ag–Cu sulfosalts, calcite and quartz. The association of zone 2 includes garnet, clinopyroxene, amphibole, carbonates, magnetite, sphalerite and subordinate hematite, chalcopyrite, cassiterite and stannite. In zone 3, amphibole, chlorite, sphalerite, chalcopyrite, arsenopyrite, cassiterite, stannite, molybdenite, native Bi, bismuthinite, Bi–Pb–Ag–Cu sulfosalts, galena, pyrrhotite, pyrite, marcasite and secondary Zn–Pb–Cu phases have been identified. The mineral association of zone 4 includes clinopyroxene, amphibole, magnetite, sphalerite, galena, chalcopyrite and pyrrhotite.

Compared to San Pietro, the orebody of Sinibidraxiu is characterised by a simpler mineralogy. Moreover, the overall textural features of each mineral appear more homogeneous throughout the different zones identified in the underground exposure (Figs 3b–4). The mineral assemblage from zones 1 to 5 includes calcite–dolomite, quartz, arsenopyrite, scheelite, galena, sphalerite, chalcopyrite, pyrrhotite, pyrite and marcasite.

The San Pietro skarn

The mineral assemblage of zone 1 includes a wide variety of calc-silicates. Garnet is abundant and forms aggregates of idiomorphic crystals with anomalous birefringence characterised by sector and concentric patterns (Fig. 5a). Clinopyroxene is the most common calc-silicate, and forms millimetre to centimetre sized idiomorphic crystals (Fig. 5c), arranged in radiating or felt-like aggregates with interstitial calcite, scheelite (Fig. 5d) and, locally, fluorite (Fig. 5e). Tiny idiomorphic inclusions are enclosed occasionally in garnet rims. Epidote, chlorite (Fig. 5h) and semi-opaque carbonate aggregates (Fig. 5b) occur where garnet is more altered, whereas amphibole-rich (Fig. 5g) aggregates are
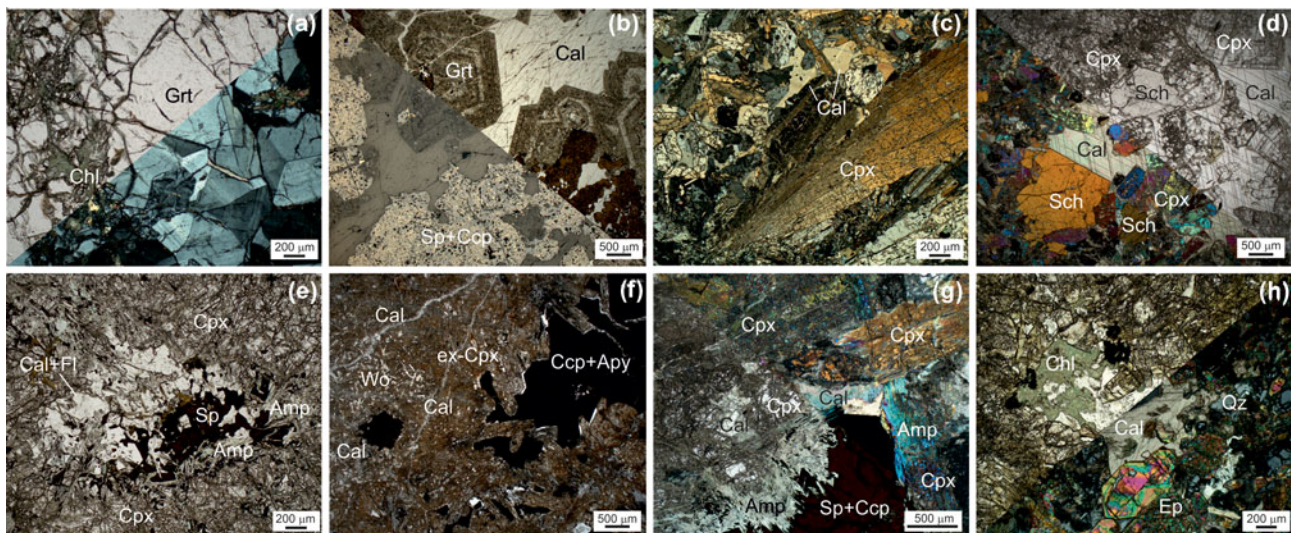

Fig. 5. Photomicrographs of prograde and retrograde mineral assemblages in the San Pietro skarn deposit: (a) fresh, anisotropic grossular garnet with minimal alteration by late epidote and chlorite (zone1, sample MTB4; transmitted light, combined parallel and crossed nicols); (b) anisotropic, partly retrocessed andradite garnet with interstitial calcite, and replacement by sphalerite (+ chalcopyrite + magnetite) aggregates (zone 2, sample MTA3D; TL-RL, PN); (c) coarse-grained euhedral diopside with interstitial calcite (zone 1, sample VMD5b; TL, XN); (d) coarse-grained euhedral diopside intergrown with scheelite and calcite (zone 1, sample VMD5b; TL, comb PN-XN); (e) felt-like aggregate of fine-grained acicular diopside with interstitial calcite and fluorite, with blebby sphalerite intergrown with actinolite (zone 2, sample MTA4; TL, PN); (f) altered diopside groundmass enveloping scarce fibrous wollastonite and cross-cut by calcite veinlets; the interstitial chalcopyrite–arsenopyrite–molybdenite aggregates are rimmed by quartz (zone 3b, sample MTB1; TL, PN); (g) fine-grained acicular actinolite rimming interstitial sulfide (sphalerite–chalcopyrite) aggregates interstitial to coarse-grained diopside (zone 1, sample VMD5b; TL, comb. PN-XN); (h) aggregates of euhedral epidote deeply replacing grossular together with fine-grained chlorite (sample MTB4; TL, comb. PN-XN). Mineral abbreviations (Warr, 2021): Grt = garnet, Cpx = clinopyroxene; Wo = wollastonite; Ep = epidote; Amp = amphibole; Chl = chlorite; Sch = scheelite; Apy = arsenopyrite; Sp = sphalerite; Ccp = chalcopyrite; Fl = fluorite; Cal = calcite; Qz = quartz.

associated with altered clinopyroxene. Wollastonite and vesuvianite are rare. Scheelite is usually found in clinopyroxene-rich facies and consists of millimetre- to centimetre-sized subhedral and fractured individuals and aggregates, associated commonly with magnetite, chalcopyrite and cassiterite (Fig. 5d and 6a). Magnetite is very common in clinopyroxene-rich facies, occasionally forming fibrous aggregates replacing hematite ('mushketovite') or, more commonly granular aggregates associated with massive chalcopyrite, at margins of scheelite. Native Bi and Bi sulfosalts can be found as tiny inclusions in altered garnet, scheelite (Fig. 6f), and calcite and as disseminations in the clinopyroxene-rich facies with scheelite and magnetite–chalcopyrite (Fig. 6a). Cassiterite occurs as subordinate individuals scattered along the contacts between scheelite and magnetite–chalcopyrite and between clinopyroxene–amphibole and sulfides (Fig. 6b–e).

In zone 2, amphibole and carbonates are widespread and overgrow clinopyroxene (e.g. Fig. 5e) and garnet (Fig. 5b). Magnetite is abundant and occurs as radial aggregates (mushketovite) typically intergrown with galena. Cassiterite occurs as rare micro-inclusions (Fig. 6m–p) in sphalerite, usually

associated with magnetite. Hematite is observed occasionally as tiny relics in sphalerite. Sphalerite forms intergrowths with the amphibole–carbonate gangue, usually enveloping magnetite and galena. It features a variably patterned 'chalcopyrite disease' (Barton and Betkhe, 1987) with minor pyrrhotite micro-inclusions (Fig. 5b and 6l–n) and stannite blebs (Fig. 6l). Bismuth phases are rare in the sphalerite-rich samples, whereas scheelite appears to be absent.

The mineral association of zone 3 features sulfide-rich aggregates intergrown in the amphibole–chlorite and carbonate matrix overgrowing clinopyroxene (Fig. 5f). The main sulfide assemblage consists of sphalerite–chalcopyrite–galena ± pyrite aggregates (zone 3a). However, a chalcopyrite ± arsenopyrite with scarce sphalerite assemblage prevails locally (zone 3b). Compared to zone 2, sphalerite is associated more commonly with pyrite rather than magnetite, and hematite, cassiterite and stannite inclusions were not found. Where chalcopyrite and arsenopyrite become more prominent (zone 3b), native Bi and Bi sulfosalts occur commonly in peculiar round or egg-shaped aggregates enclosed by molybdenite 'rings' (Fig. 6h,i) and cassiterite is overgrown
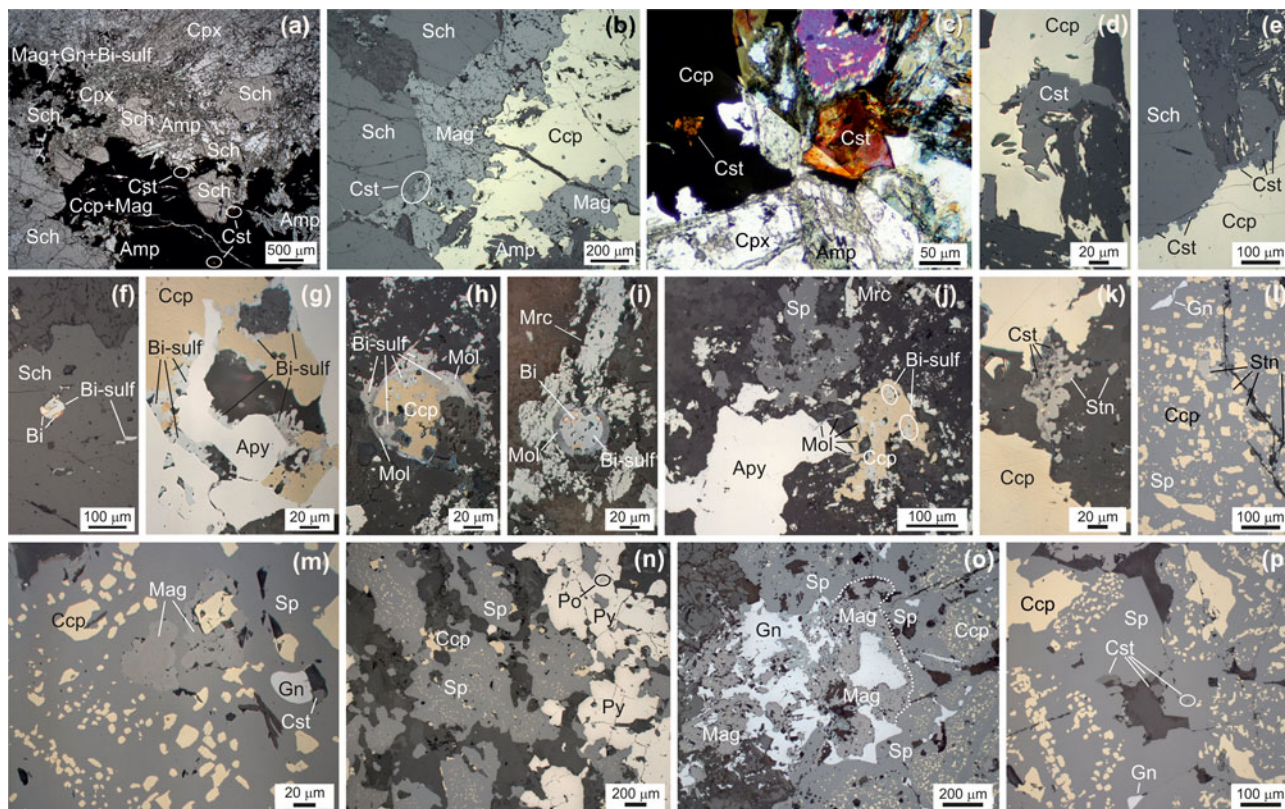

Fig. 6. Photomicrographs of ore minerals in the San Pietro skarn deposit. (a) scheelite intergrown with fibrous clinopyroxene, magnetite–chalcopyrite aggregates (with blebs of galena and Bi sulfosalts) rimmed by fibrous amphibole (zone 1, sample VMd5b; TL, PN); (b) cassiterite inclusions in magnetite intergrown with chalcopyrite and scheelite (zone 1, sample VMd5b; RL, PN); (c) cassiterite crystals associated with chalcopyrite and enclosed in the clinopyroxene matrix (zone 1, sample VMd5a TL, comb. PN-XN); (d,e). cassiterite aggregates intergrown with chalcopyrite and amphibole and rimming scheelite grains (zone 1, sample VMd5b; RL, PN); (f) native Bi and bismuthinite micro-inclusions in scheelite (zone 1, sample VMd5b; RL, PN); (g) Bi-rich sulfosalt intergrowths with chalcopyrite and arsenopyrite in the Cu-rich ore facies (zone 3b, sample MTB1; RL, PN); (h,i) ring-like molybdenite intergrown with Bi phases, chalcopyrite and marcasite, replacing pyrrhotite (zone 3b, sample MTB1; RL, PN); (j) arsenopyrite–chalcopyrite ore with Bi-rich sulfosalts (intergrown with galena), molybdenite and shredded sphalerite aggregate in carbonate-rich gangue (zone 3b, sample MTB1; RL, PN); (k) stannite crust-like aggregates replacing small cassiterite grains in the Cu-rich arsenopyrite-bearing ore facies (zone 3b, sample MTB1; RL, PN); (l) blebby stannite micro-inclusions in sphalerite with chalcopyrite disease in the Zn-rich ore facies (zone 2, sample MTA2; RL, PN); (m) sphalerite with chalcopyrite disease intergrown with granular magnetite (showing slight optical zoning), galena and cassiterite, in the pyrite-free Zn-rich ore facies (zone 2, sample MTA3; RL, PN); (n) intergrowths of sphalerite, chalcopyrite and pyrite (with few pyrrhotite relics) in magnetite-free, Zn-rich ore facies (sample MTB3; RL, PN); (o) magnetite–galena intergrowths in sphalerite-rich ore facies (zone 2, sample MTA3; RL, PN); (p) fine-grained euhedral cassiterite intergrown with sphalerite in sphalerite–magnetite ore facies (zone 2, sample MTA3; RL, PN). Mineral abbreviations (Warr, 2021): Cpx = clinopyroxene; Amp = amphibole; Sch = scheelite; Mag = magnetite; Cst = cassiterite; Bi = native bismuth; Ccp = chalcopyrite; Sp = sphalerite; Apy = arsenopyrite; Po = pyrrhotite; Bi-sulf = bismuth sulfosalts; Mol = molybdenite; Stn = stannite; Py = pyrite; Gn = galena; Mrc = marcasite.

occasionally by stannite aggregates (Fig. 6k). Galena and marcasite–pyrite overgrowing pyrrhotite are subordinate.

In zone 4 the gangue consists mostly of amphibole forming felt-like aggregates surrounding relic grains of clinopyroxene. Magnetite is widespread and occurs as mushketovite fibrous aggregates and massive aggregates, frequently enclosing anhedral galena grains with reabsorbed edges. However, galena also occurs at the edges of magnetite. Sphalerite with 'chalcopyrite disease' with the same features of zone 2 and 3 is also often found, whereas chalcopyrite and pyrite are very subordinate.

The Sinibidraxiu orebody

The gangue of the Sinibidraxiu orebody (zones 2–3) is fine-grained, semi-opaque and brownish. The characteristic

cockade-type textures observed in outcrops and hand samples consist of fibrous aggregates of fine-grained carbonates and quartz (Fig. 7a). Very fine-grained fibrous quartz is locally recrystallised to coarser clear, irregular aggregates associated generally with sulfide patches (Fig. 7b,c). Spathic calcite is commonly observed in the intergranular spaces between arsenopyrite, sphalerite and the gangue (zones 1–4). Among the ore minerals, arsenopyrite is by far the most abundant in zones 1 and 2, where it occurs as coarse-grained idiomorphic crystals (Fig. 7f). In zone 1, arsenopyrite is centimetre sized and inclusion-free, with interstitial sphalerite along fractures, whereas in zone 2 it contains abundant micro-inclusions of galena, sphalerite (Fig. 7g), and fibre-shaped inclusions of dolomite–quartz, occasionally extensively replaced by sphalerite and galena (Fig. 7g,h). Scheelite usually occurs as idiomorphic individuals (zones 1–3) associated with
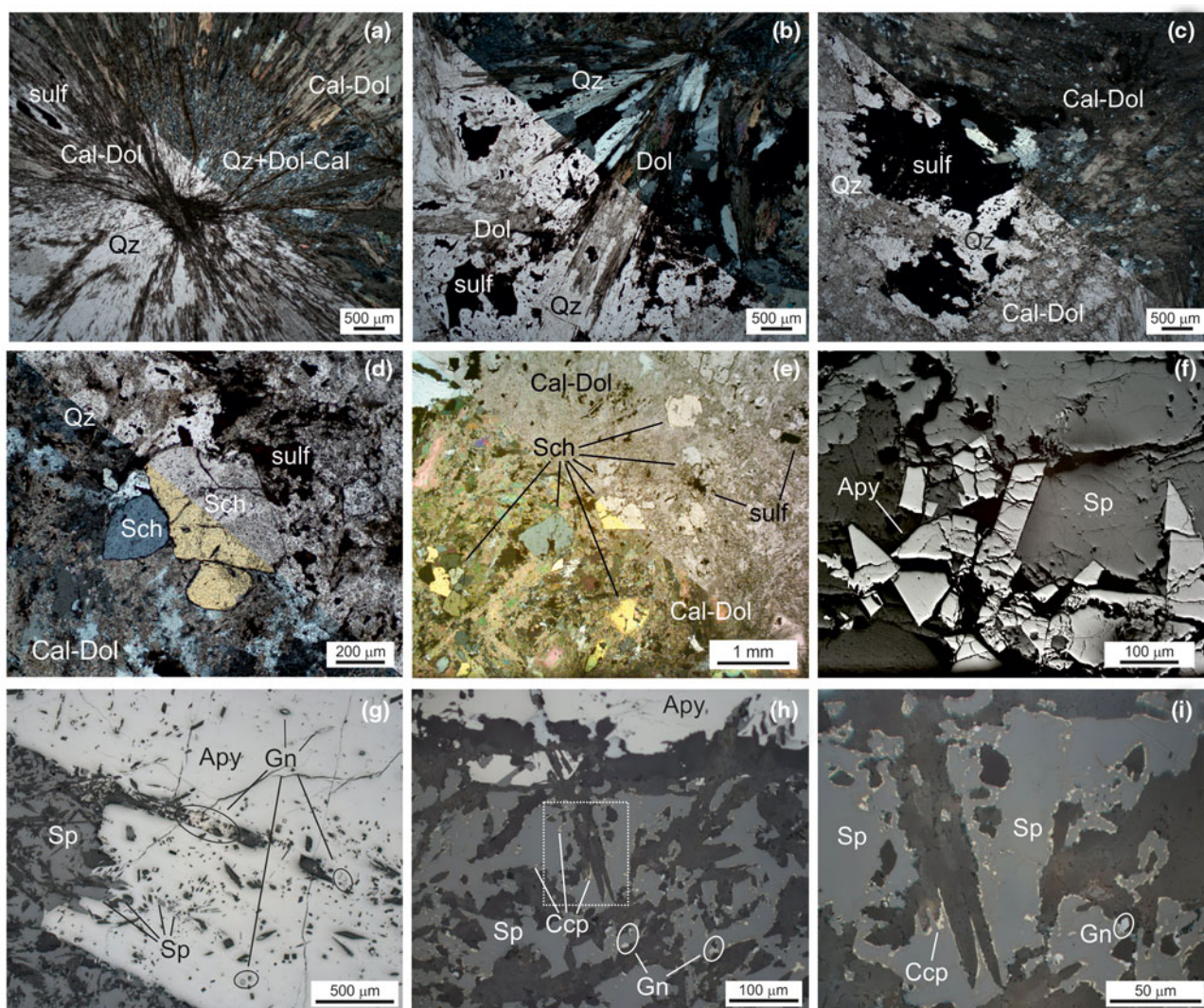

Fig. 7. Photomicrographs of gangue and ore mineral assemblages at the Sinibidraxiu skarn deposit: (a) fine-grained turbid dolomite and quartz replacing fibrous aggregates with interstitial sulfides enveloped in quartz (sample SB-c1; TL, comb. PN-XN); (b,c) sulfide patches interstitial to, and overgrowing, fibrous aggregates extensively replaced by fine-grained dolomite–quartz (sample SB-d; TL, comb. PN-XN); (d,e) idiomorphic scheelite crystals disseminated in the dolomite–quartz matrix (zone 3, samples SB11A and SB11B; TL, comb. PN-XN); (f) idiomorphic, fractured arsenopyrite surrounded by sphalerite (zone 2, sample SB8E; RL, PN); (g) arsenopyrite containing micro-inclusions of sphalerite, of galena and very abundant inclusions of the fibrous gangue (zone 2, sample SB12; RL, PN); (h) sphalerite–arsenopyrite border zone, rich in fibrous inclusions (zone 2, sample SB12; RL, PN); (i) close-up view of contacts between sphalerite and carbonate–quartz fibres: zones of higher transparency and dissemination of chalcopyrite and galena micro-grains mark the sphalerite–matrix contacts and microfractures (zone 2, sample SB12; RL, PN). Mineral abbreviations (Warr, 2021): Cal = calcite; Dol = dolomite; Qz = quartz; Sch = scheelite; Apy = arsenopyrite; Sp = sphalerite; Ccp = chalcopyrite; Gn = galena; Po = pyrrhotite; Py = pyrite; sulf = sulfides.

arsenopyrite (zone 1) and locally arranged in oriented seams and disseminations in the carbonate–quartz gangue (zones 2–3; Fig. 7d,e). Pyrrhotite, typically altered to fine-grained pyrite–marcasite intergrowths, has been observed occasionally at the edges of arsenopyrite (zone 2) or enclosed in chalcopyrite–galena aggregates. Sphalerite occurs as aggregates at the margins and in fractures of arsenopyrite (zone 1–2; Fig. 7f) and as interstitial to, and enveloping, the carbonate–quartz gangue (zones 2–3–4; Fig. 7g–i). In the first association, chalcopyrite and pyrrhotite inclusions are rare, whereas in the latter chalcopyrite–galena and subordinate pyrrhotite–pyrite–marcasite micro-inclusions are more common. Inclusions are distributed irregularly and concentrated at the sphalerite margins along the contact with the carbonate–quartz gangue (zone 2; Fig. 7i). This feature is also accompanied by a more pronounced transparency of sphalerite. Galena occurs as small, disseminated blebs and as large, network-like aggregates surrounding arsenopyrite crystals (zone 2), and disseminated variably elsewhere in the gangue and intergrown with sphalerite (zones 2–3–4; Fig. 7g–i). Chalcopyrite and pyrite–marcasite are interstitial to the carbonate–quartz gangue.

The paragenetic schemes for the San Pietro and Sinibidraxiu mineralisation, as deduced by the mineral assemblages and related textural features, are presented in Fig. 8.

Mineral compositions

Samples from San Pietro and Sinibidraxiu were investigated initially by SEM using energy dispersive spectroscopy (EDS) for semi-quantitative analysis and compositional maps, whereas quantitative mineral compositions were determined by electron probe microanalyses (EPMA) and laser-ablation inductively coupled mass spectrometry (LA-ICP-MS) on a selected set. Due to its paragenetic complexity, a larger set of samples from San Pietro has been analysed. The mineral composition of skarn and ore minerals (Tables S1–14 in Supplementary materials) are presented below for each mineral group, with comparisons for ore minerals between the different localities.

Skarn minerals

Garnet

Garnet crystals from San Pietro, are characterised either by concentric or sector birefringence (Table S1). The garnets belong to the grossular–andradite solid solution, though with a clear compositional distinction (Fig. 9a,b) between the sector zoned MTB4 garnet (Fig. 5a), enriched variably in the grossular end-member (82.4–33.7% Grs, 63.2–13.1% Adr and 3.0–1.6% Sps), and the concentrically zoned garnet from zone 2 (MTA3d sample; Fig. 5b), which plots close to the pure andradite end-member (99.6–93.5% Adr; 4.3–0% Grs; 3.0–0.4% Sps). In the MTB4 garnet the variations in the grossular, or Al_2O_3, component reflect distinct core-to-rim zoning (Fig. 9b). Of the accessory elements, Ti (Fig. 9c) also displays a variable distribution in the MTB4 garnet compared to the restricted field for the MTA3d andradite, whereas Mn and Sn display similar ranges of variation in the two main garnet varieties (Fig. 9d,e). The garnet sporadically displays W contents above the EPMA detection limit (2000 ppm). The few data for the rare garnet in pyroxene-dominated skarn facies of zone 1 (sample VMd5b) show affinities with the grossular-enriched population. Notably, each garnet is Sn-enriched, with some maximum contents over 1 wt.% SnO_2. In the element-distribution X-ray maps and profiles across the
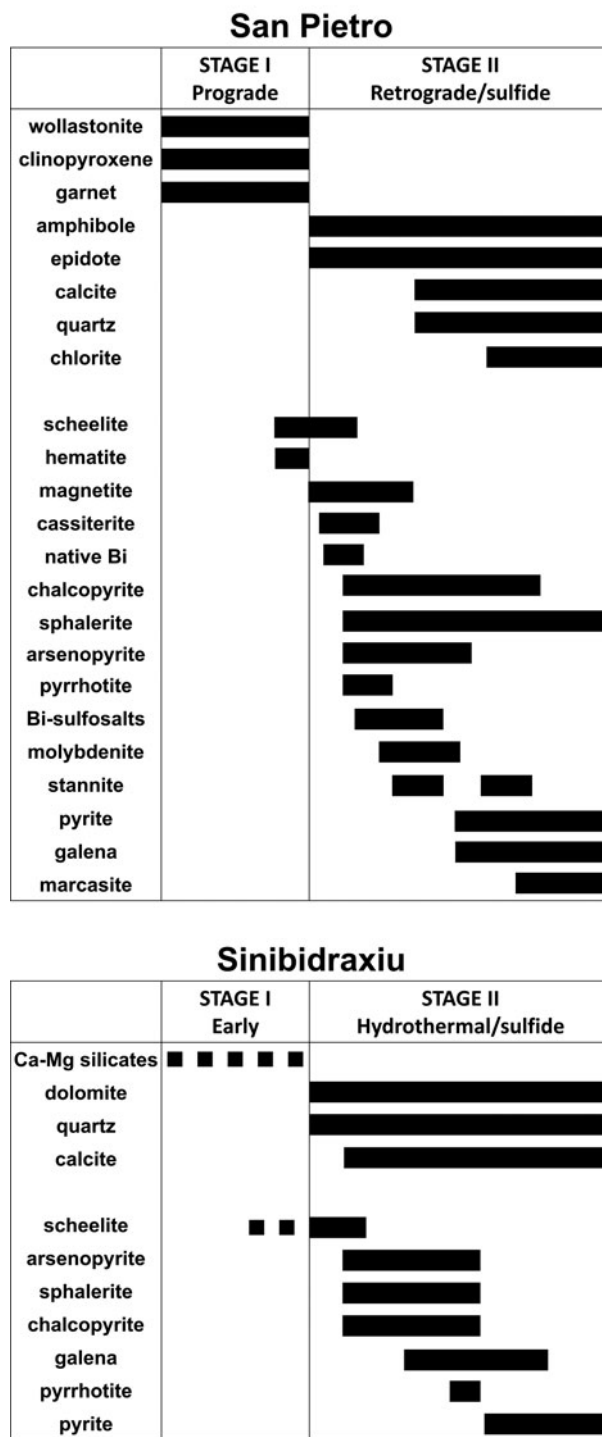

Fig. 8. Paragenetic sequence of the San Pietro and Sinibidraxiu orebodies.

garnet (Fig. 10), the Sn enrichments appear to correlate positively with Fe and negatively with Ti.

Clinopyroxene

All San Pietro clinopyroxene from zone 1 (Table S2), independently of grain size, are essentially diopside (Fig. 11a), with low Mn contents (rarely > 1 wt.% MnO; Fig. 11b,c). The Sn contents commonly exceed the microprobe detection limit of 350 ppm, and range from frequently >0.1 wt.% to 0.36 wt.% SnO_2 (Fig. 11c).
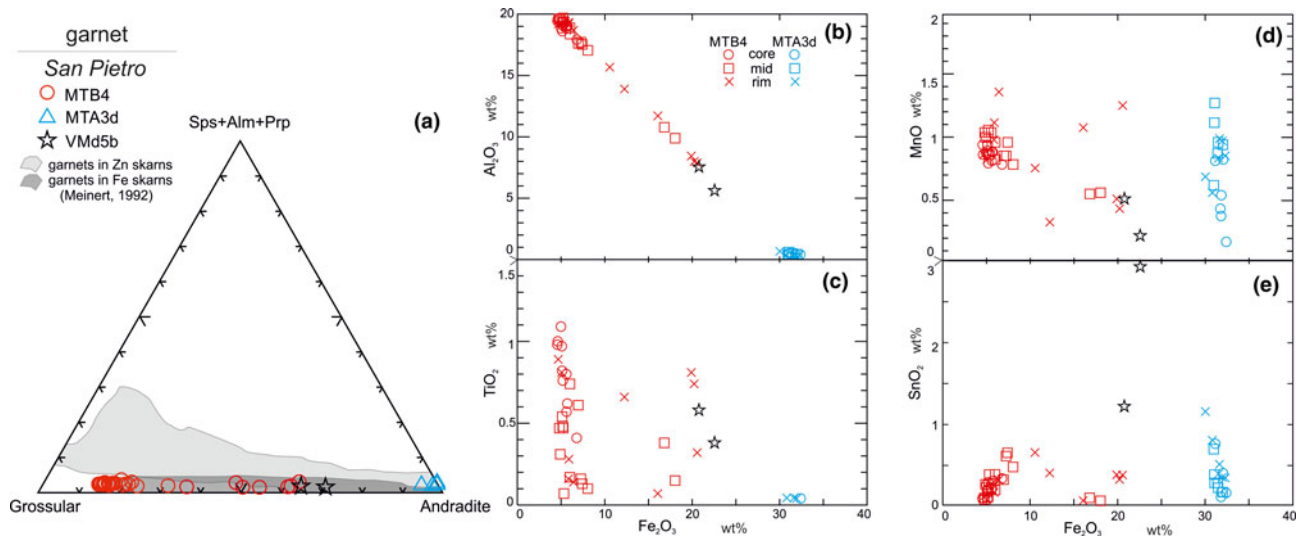
Fig. 9. Ternary (a) and binary compositional diagrams (b–e) for garnet from garnet-rich (MTB4, MTA3d) and garnet-poor (VMd5b) samples from the San Pietro skarn. Symbols in the binary diagrams represent data points from cores to rims.
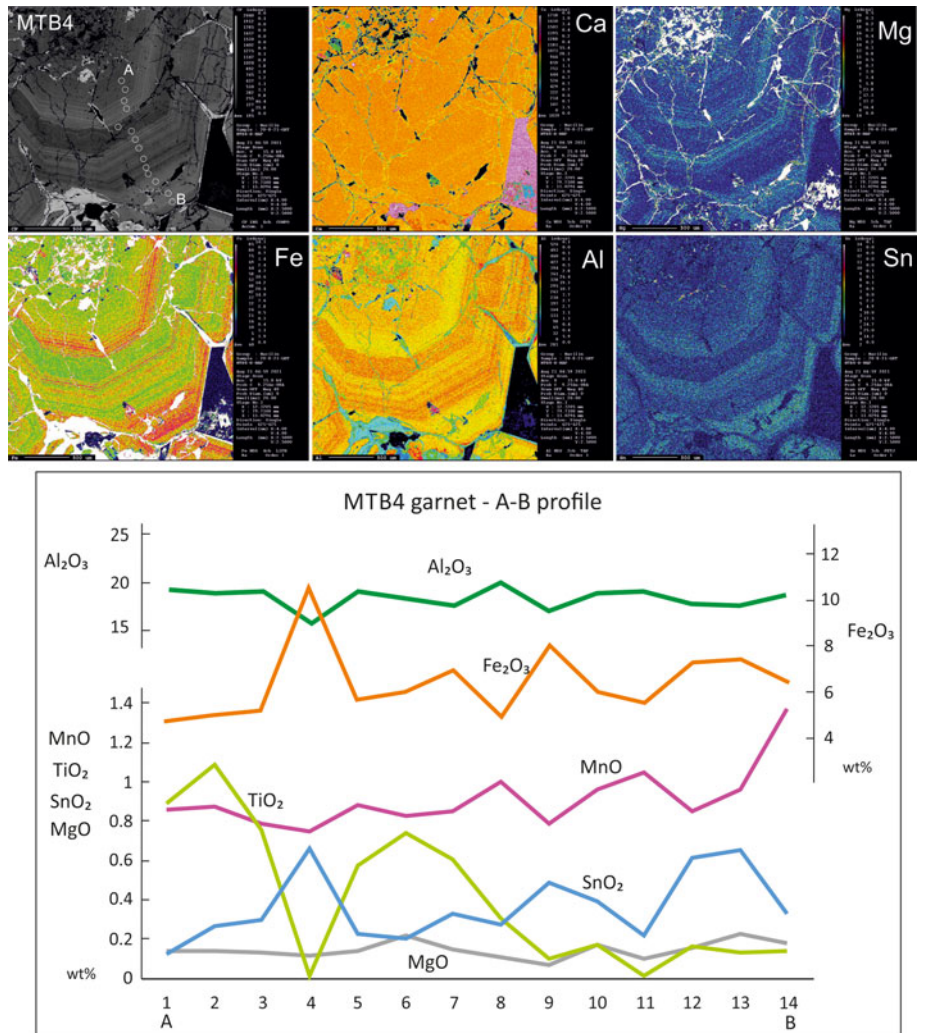

Fig. 10. Element distribution EPMA X-Ray maps from core to rim for one of the sector-zoned garnets in sample MTB4. The A–B profile in the BSE image shows the location of analytical points for data given in the graph.
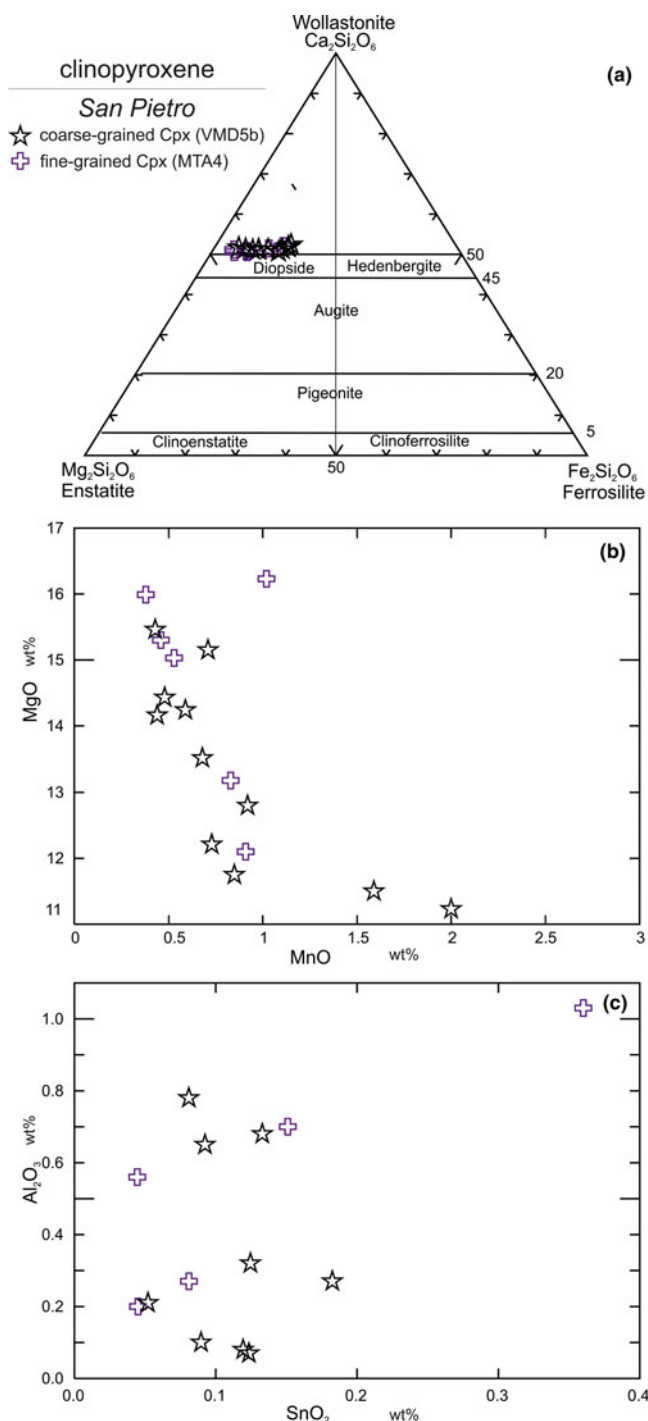
Fig. 11. Ternary (a) and binary compositional diagrams (b,c) for clinopyroxene from the San Pietro skarn, with grain size ranging from coarse (sample VMd5b) to fine (sample MTA4).

Amphibole
The limited compositional data (Table S3) for amphibole replacing coarse and fine grained clinopyroxene in zone 1 of the San Pietro skarn indicates they are all actinolite (Fig. 12a,b) with Sn contents up to 0.13 wt.% in some examples.

Epidote and chlorite
Epidote and minor chlorite occur as replacement phases on garnet in the San Pietro skarn. Epidote (Table S4) belongs to the Fe-rich epidote end-member, with a minor piemontite component (Pmt$_{5-15}$) and notable concentrations of Sn (often > 0.1 wt.% SnO$_2$), probably inherited from the garnet substrate. Preliminary data for associated fine-grained chlorite aggregates (Table S5) indicate clinochlore compositions (e.g. Deer *et al.*, 1962), with low Sn, though Mn contents are similar to the original garnet (~1 wt.% MnO).

Ore minerals (sulfides and oxides)

Sphalerite
Sphalerite is the main sulfide ore mineral in the San Pietro skarn and displays variable compositional features (Table S6). On the basis of the Fe contents, three groups of sphalerite are distinguished (Fig. 13a). The Fe-rich group, with 11–13 wt.% Fe, is represented by sphalerite in the sphalerite–chalcopyrite–galena ± pyrite aggregates (zone 3a; sample MTB3) of San Pietro and by the cores of sphalerite from Sinibidraxiu (zone 3; sample SB12). The mildly ferriferous group, containing 4–8 wt.% Fe, corresponds to sphalerite of the chalcopyrite–scheelite-rich (zone 1; sample VMd5b), magnetite-rich (zones 2–3b; samples MTA3, MTA2, MTB1), and the chalcopyrite-rich (zone 3a; sample MTB1) assemblages of San Pietro. A third, Fe-poor group, characterised by 1.7–0.5 wt.% Fe, belongs to the chalcopyrite-rich assemblage of San Pietro (zone 3a), and the inclusion-rich rims of Sinibidraxiu sphalerite (zones 3–4, sample SB12). Cadmium values in San Pietro sphalerite (av. 1 wt.%) show a negative correlation with Zn (Fig. 13b), with the most Fe-rich sphalerite displaying the highest Cd contents (up to 1.7 wt.%). In contrast, Cd contents of Sinibidraxiu sphalerite are markedly lower (up to 0.5 wt.%) and unrelated to their Fe contents. A positive correlation with Fe, involving all analysed grains, can be observed for Mn (Fig. 13c), with sphalerite from Sinibidraxiu attaining the highest Mn contents (0.4–0.5 wt.%). The San Pietro sphalerite appear to be mildly cobaltiferous, whereas Ni rarely exceeds detection limits. Cobalt-bearing sphalerite occurs especially in the scheelite–chalcopyrite (zone 1; sample VMd5b) and in the sphalerite–magnetite ore facies (zones 2–3b; samples MTA3, MTA2, MTB1), where Co is commonly above the 350 ppm detection limit and may attain peak values >0.3 wt.% Co. Sporadic Co enrichments are also found in Sinibidraxiu sphalerite. Overall, both San Pietro and Sinibidraxiu sphalerite has low indium and tin contents. Indium is never above the EPMA detection limit, whereas Sn is found as sporadic enrichments (up to 0.27 wt.% Sn) mainly in the San Pietro sphalerite of the sphalerite–magnetite ore facies (zones 2–3b; samples MTA3, MTA2, MTB1). This is probably related to micro-inclusions of cassiterite and stannite. Germanium was detected sporadically below 0.1 wt.% in the San Pietro sphalerite cores of the chalcopyrite–scheelite (zone 1; sample VMd5b) and the sphalerite–magnetite ore facies (zones 2–3b; samples MTA3, MTA2, MTB1). Bismuth displays variable, although commonly high, concentrations (up to 0.3 wt.% Bi) in sphalerite from San Pietro and Sinibidraxiu (Fig. 13d); Ag is typically below the detection limit and locally up to 0.14 wt.%. Bismuth and Ag concentrations are coupled with variable Pb contents (up to 0.2 wt.%). The Bi, Ag and Pb contents of sphalerite are probably related to the presence of (sub-) micro-inclusions of the Bi–Pb–Ag–Cu sulfosalts (Lockington *et al.*, 2014), similar to those identified in the San Pietro ore (see below).
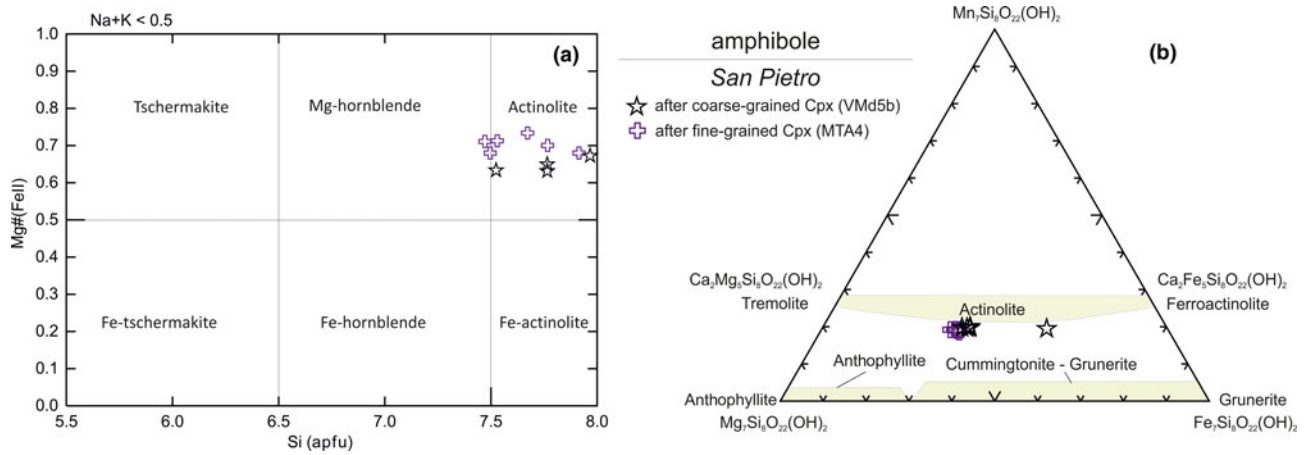
Fig. 12. Amphibole compositions of the San Pietro skarn according to the binary classification diagram (a) by Leake *et al.* (2003) and to the ternary diagram for Fe–Mn amphiboles (b) by Hawthorne *et al.* (2012).

Bi-bearing sulfosalts

Samples from San Pietro show a complex association of accessory Cu–Ag–Pb–Bi sulfosalts (Table S7), represented in the Ag + Cu *vs.* Bi + Sb *vs.* Pb ternary diagram (Fig. 14; Ivashchenko, 2021; Damian *et al.*, 2008; Voudouris *et al.*, 2008). On the basis of their different Bi–Ag–Pb–S quantitative ratios (Moelo *et al.*,

2008 and references therein), bismuthinite (Bi_2S_3), 'phase 88.6' ($Cu_{0.33}Pb_{0.33}Bi_{7.67}S_{12}$, Ciobanu and Cook, 2000), pekoite ($PbCuBi_{11}S_{16}Se_2$), cosalite ($Pb_2Bi_2S_6$), salzburgite–paarite ($Cu_{1.6}Pb_{1.6}Bi_{6.4}S_{12}$–$Cu_{1.7}Pb_{1.7}Bi_{6.3}S_{12}$), gustavite ($PbAgBi_3S_6$), berryite ($Cu_3Ag_2Pb_3Bi_7S_{16}$), xilingolite–lillianite ($Ag_xPb_{3-2x}Bi_{2+x}S_6$–$Pb_3Bi_2S_6$) ourayite ($Pb_4Ag_3Bi_5S_{13}$) and cupropavonite
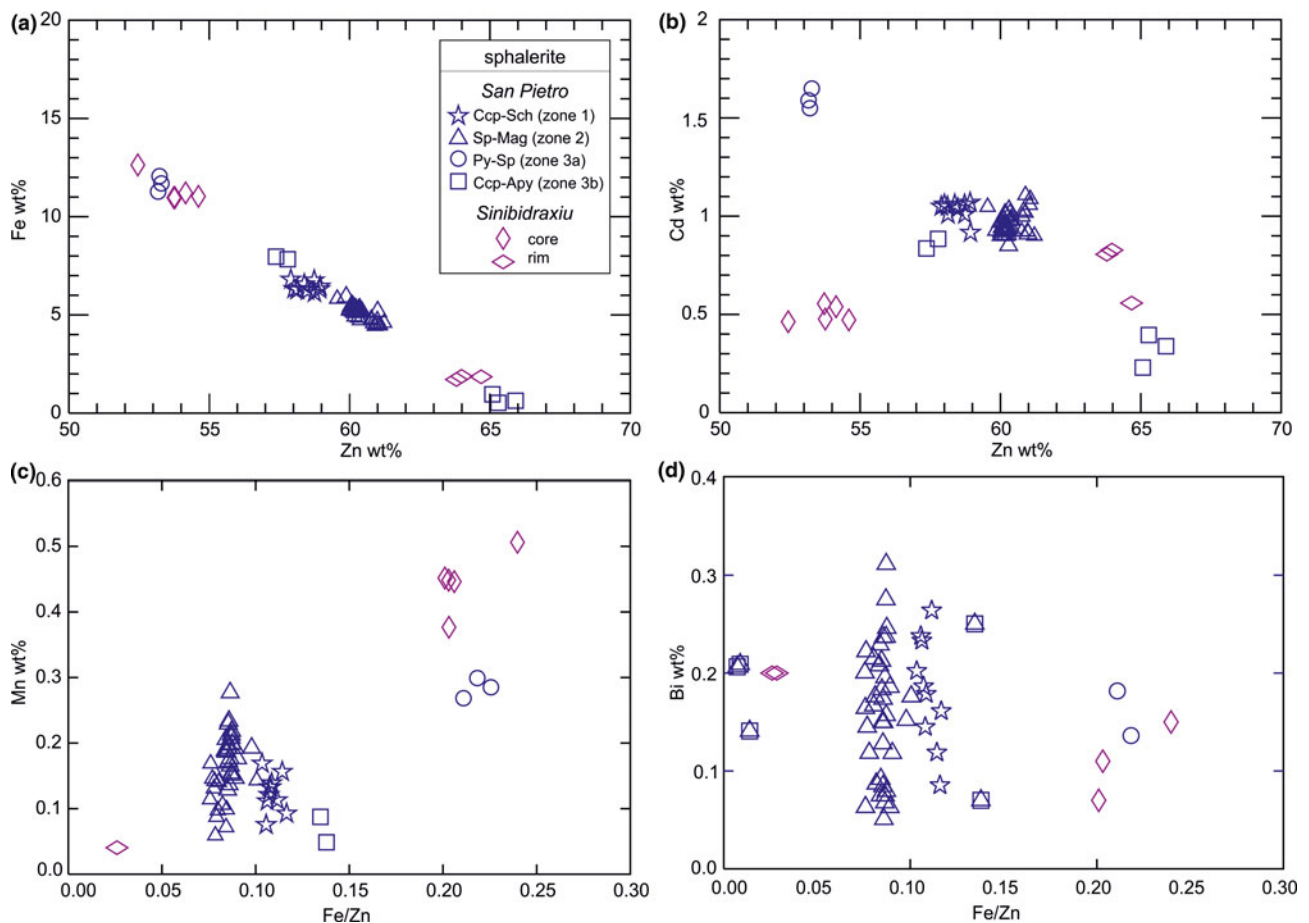

Fig. 13. Plots of sphalerite compositions (wt.%) for the San Pietro and Sinibidraxiu skarn deposits: (a,b) binary diagrams of major (Zn, Fe and Cd); and (c–f) selected accessory components (Mn, Bi) *vs.* Fe/Zn. The different symbols for San Pietro sphalerite correspond to the zones 1–2–3a–3b of the orebody; the symbols for Sinibidraxiu sphalerite refer to the core and rim composition.
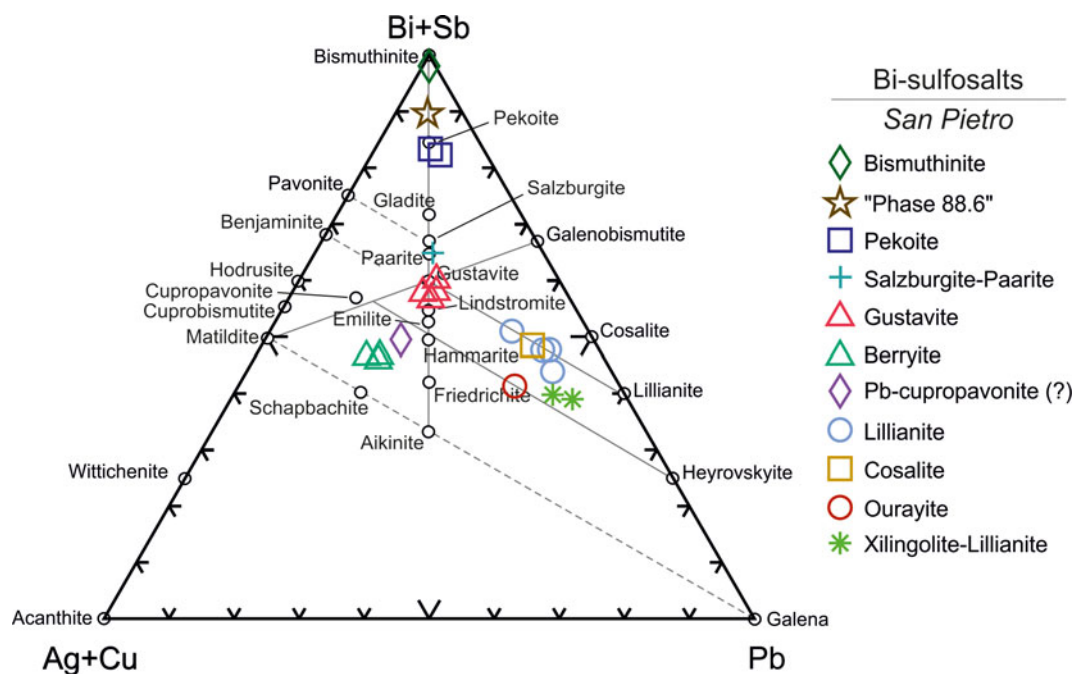
Fig. 14. Ternary diagram representing the compositions of the Bi-bearing sulfosalts detected in zone 3 of the San Pietro skarn (modified after Ivashchenko, 2021; Damian *et al.*, 2008; Voudouris *et al.*, 2008).

$(Cu_{0.9}Ag_{0.5}Pb_{0.6}Bi_{2.5}S_5)$ were identified. Bismuthinite occurs in both chalcopyrite–scheelite (zone 1; sample VMd5b) and sphalerite–pyrite ore facies (zone 3a; sample MTB3), whereas the other Bi phases occur in the chalcopyrite-rich facies only (zone 1–3a; samples VMd5b-MTB1). All the Bi phases display a mildly seleniferous character, with average Se contents of 0.58 wt.% and maximum at 1.5 wt.% Se. Maximum values were recorded in bismuthinite, which occasionally contains Pb (4 wt.%) or Cu (1 wt.%) contamination due to intergrowths with galena or chalcopyrite. Pekoite $(PbCuBi_{11}S_{16}Se_2)$ is characterised by localised Sn maximum contents of 0.18 wt.%, probably due to contamination by the common stannite blebs in the chalcopyrite host. A phase with a composition intermediate between bismuthinite and pekoite was identified as the 'phase 88.6' $(Cu_{0.33}Pb_{0.33}Bi_{7.67}S_{12}$; Moelo *et al.*, 2008 and references therein). One spot analysis showed a correspondence with the composition of salzburgite–paarite $(Cu_{1.58–1.67}Fe^{2+}_{0.03–0.01}Pb_{1.65–1.72}Bi_{6.38–6.3}S_{12–12.06})$. Cosalite $(Pb_2Bi_2S_6)$ has a Pb deficit (1.73 atoms per formula unit) coupled with a slight enrichment in Cu (0.35 apfu) which may be attributed to a Pb^{2+}–Cu^+ coupled substitution with Bi^{3+} (Moelo *et al.*, 2008). At least five Ag-bearing sulfosalts were detected, with Ag ranging between 3.3 and 7.8 wt.%. Spots on gustavite $(PbAgBi_3S_6)$ reveal variable Cu enrichments (locally >1 wt.%). Gustavite and berryite $(Cu_3Ag_2Pb_3Bi_7S_{16})$ display the highest Ag contents, with similar contents averaging 7.4 wt.% Ag. Lillianite was recognised on the basis of the $Ag_xPb_{3–2x}Bi_{2+x}S_6$ structural formula proposed by Moelo *et al.* (2008), whereas phases corresponding closer to the lillianite simplified formula $(Pb_3Bi_2S_6)$ were attributed generically to the xilingolite–lillianite polymorphs. The other identified phases, though with a certain degree of uncertainty, include ourayite $(Pb_4Ag_3Bi_5S_{13})$ with a Pb-enrichment over Ag $(Pb_{5.08}Ag_{1.88}Bi_{4.95}S_{13})$, and cupropavonite $(Cu_{0.9}Ag_{0.5}Pb_{0.6}Bi_{2.5}S_5)$ with an excess of 0.3 apfu of Pb over Cu $(Cu_{0.68}Ag_{0.65}Pb_{0.94}Bi_{2.23}S_5)$.

Arsenopyrite, pyrrhotite and pyrite

Arsenopyrite (Table S8) approaches its theoretical composition with slight variations on the As contents (33.2–33.9 at.% at San Pietro; 32.4–33.1 at.% at Sinibidraxiu) and more pronounced variations for Fe, particularly in the San Pietro samples (28.3–33.6 at.% Fe), compared to Sinibidraxiu (31.2–34 at.% Fe). The most significant accessory element in the Fe-poor arsenopyrites is Co, with higher average values at San Pietro (1.8 wt.%, maximum 5.4 wt.% Co) compared to Sinibidraxiu (average 0.61 wt.%, maximum 3.3 wt.% Co). Contents of Se occasionally attain 0.2 wt.%. Pyrrhotite and pyrite from San Pietro and Sinibidraxiu (Table S8) are low in Se (close to or below the 200 ppm detection limit), however tend to be Co-bearing: up to 0.2 and 0.16 wt.% Co for San Pietro pyrrhotite and pyrite, respectively, and 0.12 wt.% Co for the Sinibidraxiu pyrite. The high Bi and Pb contents (> 0.1 wt.%), in pyrite and pyrrhotite from San Pietro and in pyrrhotite from Sinibidraxiu, might result from micro-inclusions of Bi and Pb phases.

Chalcopyrite

Chalcopyrite occurs in variable amounts in the various ore facies of the San Pietro skarn, although its composition appears to be rather constant (Table S9). Small amounts of Zn (1–1.7 wt.%) are recorded only in chalcopyrite inclusions in sphalerite. Cobalt, Pb and Te are detected sporadically, whereas Bi is commonly well above the EPMA detection limit (up to 0.28 wt.% Bi).

Galena

The analysed galena from Sinibidraxiu and San Pietro (Table S10) contain Bi, Ag and Se as the main trace elements. Of these, Bi is the most abundant (up to 1.48 wt.% in San Pietro) and detected in all analyses from both localities, although galena from Sinibidraxiu exhibits lower contents relative to San Pietro. Selenium enrichments characterise only galena from San Pietro

(from 0.06 to 0.4 wt.% Se). A maximum value of 0.12 wt.% Te was detected in galena from San Pietro, and is probably due to micro-inclusions of Bi tellurides (George *et al.*, 2015).

Stannite

The general compositions of stannite from the San Pietro skarn (Table S11) are compatible with mildly Zn-bearing phases within the solid solution between pure stannite (Cu_2FeSnS_4) and kësterite (Cu_2ZnSnS_4) end-members. Figure 15 shows that stannite data plot into two separate clusters: the blebs from the chalcopyrite–arsenopyrite ore facies (zone 3b; sample MTB1) all plot close to the stannite end-member, whereas the more dispersed cluster plotting closer to the ferrokësterite end-member ($Cu_2(Fe,Zn)SnS_4$) corresponds to blebs from the sphalerite–magnetite ore facies (zone 2; sample MTA2). The main trace elements of the San Pietro stannite, which is devoid of In, are represented by Te (avg. 0.3 wt.%), Bi (avg. 0.13 wt.%) and Se (avg. 0.1 wt.%), which are recorded consistently in all analyses, and by Pb peaks (below 0.2 wt.%).

Cassiterite

The compositions of cassiterite (Table S12) were determined by EMPA on small single grains occurring in the chalcopyrite–scheelite (zone 1; sample VMd5b), chalcopyrite–arsenopyrite (zone 3a; sample MTB1) and sphalerite–magnetite (zone 2–3b; samples MTA2-MTA3) ore facies of San Pietro. Indium contents in cassiterite attain 0.3 wt.% In_2O_3 with an average of 0.14 wt.%. Other detected minor and trace elements are Fe, Zn and Te. Iron (expressed both as ferrous and ferric oxide in Table S12) occurs in variable amounts, from below 0.1 up to 2.9 wt.% Fe_2O_3, unevenly distributed in cassiterite grains from different ore facies (Fig. 16b). Zinc shows distribution trends similar to In (Fig. 16a), whereas Te contents (Fig. 16c) were only detected in the cassiterite grains belonging to the sphalerite–magnetite and chalcopyrite–arseno-pyrite ore facies, where accessory stannite (also Te bearing) is widespread.

Scheelite

Analyses on scheelite were performed by EPMA and LA-ICP-MS on samples from San Pietro (zone 1; sample VMd5b) and Sinibidraxiu (zone 3; sample SB11). In terms of major elements, the scheelite crystals are compositionally similar in both sites (Table S13), without appreciable zoning. However, subtle-to-remarkable differences were revealed by LA-ICP-MS data (Table S14), particularly for Mo, Y and REE contents. The San Pietro scheelite is moderately enriched in Mo (ranging between 737 and 2467 ppm, avg. 1593 ppm Mo) compared to Sinibidraxiu scheelite (ranging between 6.3 and 42 ppm, avg. 21 ppm Mo) with no rim-to-core variations (Fig. 17a). Yttrium and REE show an opposite trend, as the $\Sigma REE+Y$ contents in the Sinibidraxiu scheelite are remarkably higher (from 62 to 564 ppm, avg. 386 ppm) than those in the San Pietro scheelite (range 3–31 ppm, av. 19 ppm). The Y/Ho ratios are markedly higher at Sinibidraxiu than in San Pietro and they exhibit a good linear correlation (Fig. 17b). The chondrite-normalised REE distribution patterns for both San Pietro and Sinibidraxiu scheelite show a seagull-wing-like shape with distinct negative Eu anomaly (Fig. 17d). The Eu anomaly (Eu/Eu* = Eu/[(Gg·Sm)$^{1/2}$]) is slightly more pronounced for the Sinibidraxiu scheelite (average Eu/Eu* of 0.06 and up to 0.16) compared to the San Pietro scheelite (avg. of 0.24 and up to 0.35). Moreover, the San Pietro scheelite displays profiles characterised by light
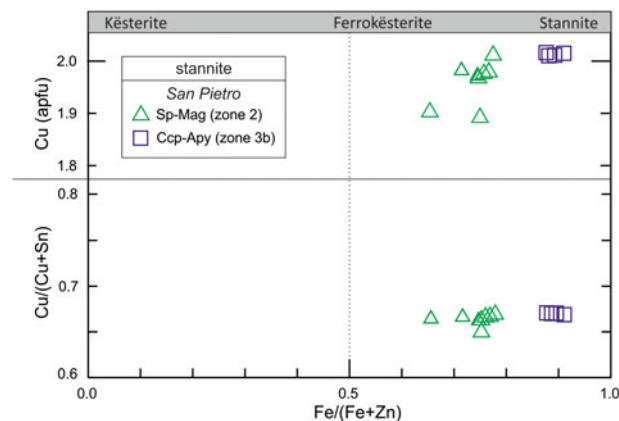

Fig. 15. Compositions of stannite from zones 2 and 3b of San Pietro skarn as functions of Cu (apfu) and Cu/(Cu + Zn) *vs*. Fe/(Fe + Zn) (after Petruk, 1973).
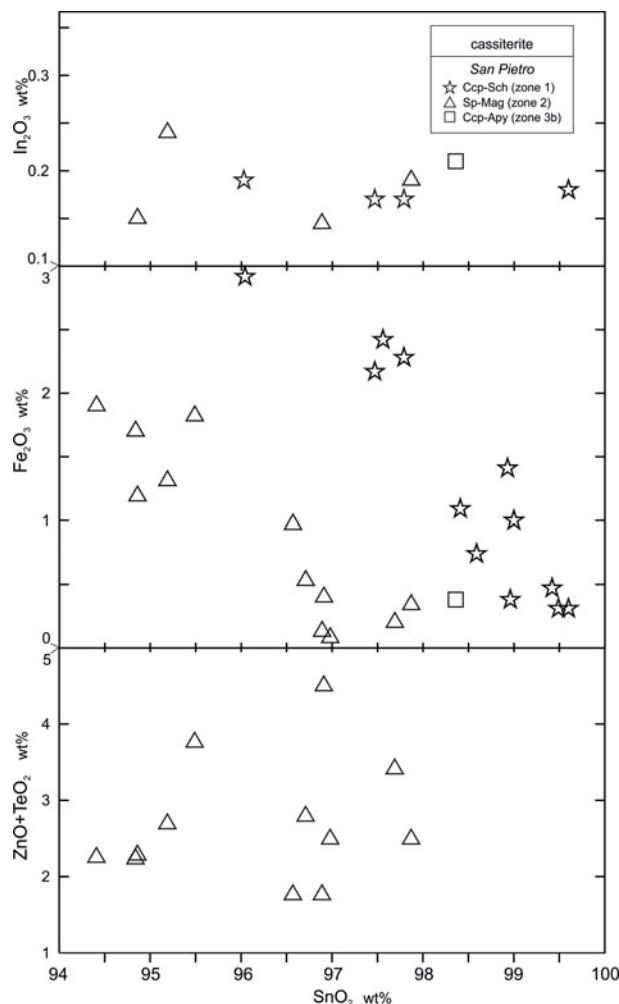
Fig. 16. Compositions of accessory elements (wt.% oxides) in cassiterite grains from the chalcopyrite–scheelite (zone 1), sphalerite–magnetite (zone 2) and chalcopyrite–arsenopyrite (zone 3b) ore facies of the San Pietro skarn.

versus heavy REE (LREE *vs*. HREE) enrichments. Other minor differences in trace-element concentrations involve Nb-Ta and As. Niobium, paired with Ta, is mildly enriched in the San Pietro scheelite (avg. 8.8 ppm Nb and 0.07 ppm Ta) compared to

Fig. 17. Binary, spider and triangular composition diagrams for scheelite from the Sinibidraxiu and San Pietro ores: (a) Mo *vs.* Eu/Eu* (modified after Poulin *et al.*, 2018); (b) Y *vs.* Ho (modified after Ding *et al.*, 2018); (c) Sr *vs.* Eu/Eu* (modified after Poulin *et al.*, 2018); (d) chondrite-normalised (Sun and McDonough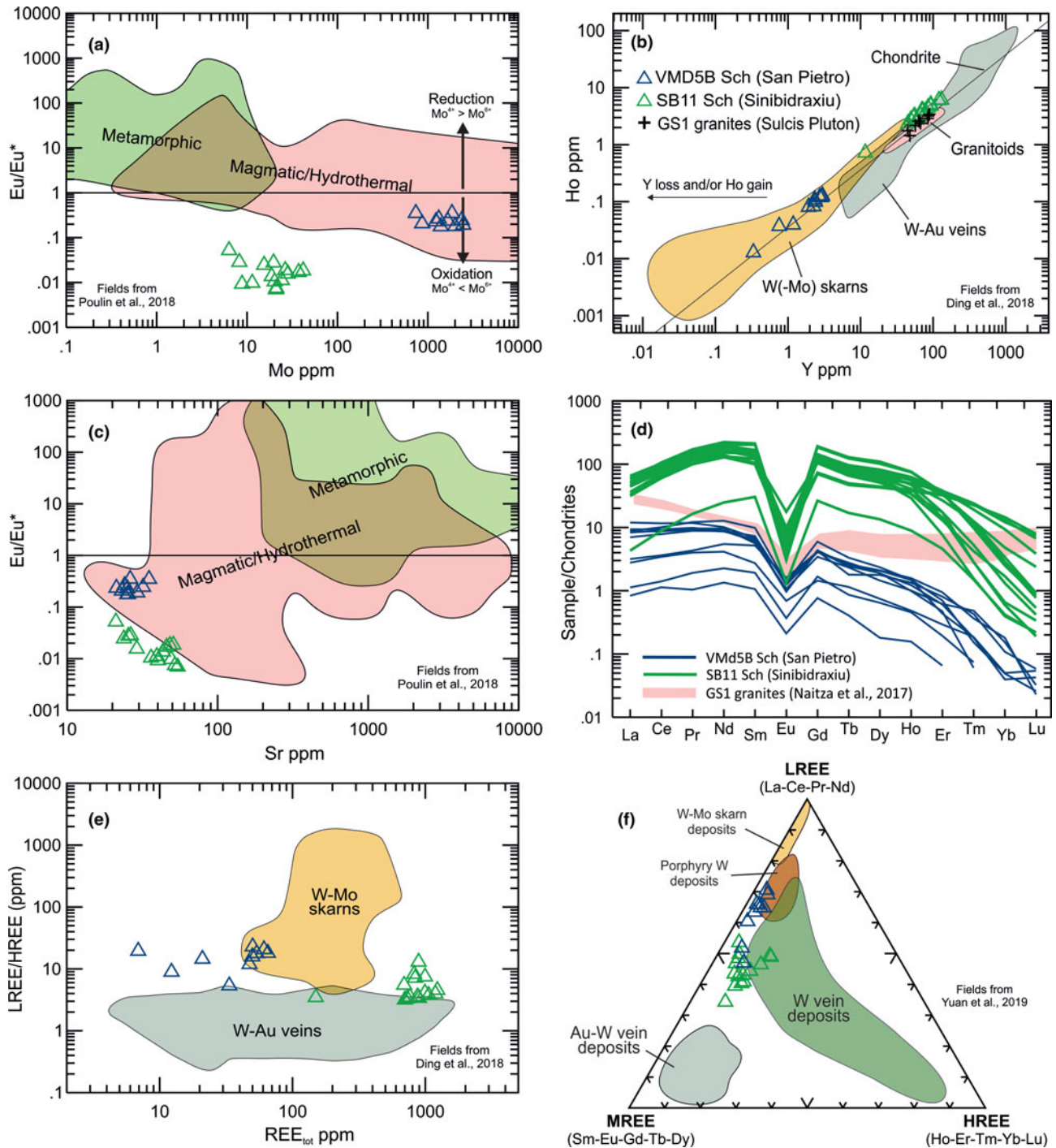, 1989) REE distribution patterns and comparison with the GS1 granite in the Sulcis area (modified after Naitza *et al.*, 2017); (e) total REE *vs.* LREE/HREE (modified after Ding *et al.*, 2018); (f) normalised LREE–MREE–HREE contents (modified after Song *et al.*, 2014, Yuan *et al.*, 2019).

Sinibidraxiu (avg. 2.5 ppm Nb and 0.015 ppm Ta). Arsenic contents are generally low, although slightly more enriched in the San Pietro scheelite (from 2.4 to 8.24 ppm, avg. 4.5 ppm As) compared to the Sinibidraxiu scheelite, where As is typically below the detection limit and rarely exceeds 1 ppm. Scheelite from both sites are Sr poor (average Sr values below 40 ppm, Fig. 17c) and Mn poor. Manganese is slightly more enriched (avg. 2.25 ppm Mn) in the Sinibidraxiu scheelite compared to San Pietro (avg. 0.54 ppm Mn).

Discussion

The orebodies at the San Pietro and Sinibidraxiu mines display clear differences in the skarn mineralogy and ore mineral associations. The San Pietro orebody is characterised by multi-stage formation of a prograde assemblage (garnet, clinopyroxene, hematite, scheelite), affected by retrograde alteration (amphibole, epidote, chlorite) and oxide and sulfide mineralisation (magnetite,

cassiterite, Bi phases, Cu–Fe–Zn sulfides, molybdenite, stannite and galena). This succession of temperature- and time-controlled assemblages is different at Sinibidraxiu. Here, an early-stage calc-silicate assemblage, forming radiate and fibrous aggregates, was probably extensively replaced by a hydrothermal assemblage (carbonates–quartz), coinciding with the ore mineral deposition (arsenopyrite, scheelite, sphalerite). However, several common features allow us to bring the two ore deposits into a common framework. These are: (1) a similar metallogenic signature, with the occurrence in both ores of variable amounts of scheelite, as well as arsenopyrite, sphalerite and other base metal sulfides (chalcopyrite, galena, pyrrhotite, pyrite); (2) a similar role of the pre-existing structural framework in focusing fluids during the mineralising processes; and (3) allegedly, the same granite intrusion source (the GS1 intrusive suite of Conte *et al.*, 2017). However, regardless of these similarities, an important difference exists in the host rocks. At San Pietro, the skarn orebody formed at the contact between a siliciclastic unit and a carbonate formation whereas at Sinibidraxiu the orebody is confined entirely to the carbonate host. At both localities, the carbonate rocks are metamorphosed to marbles. The migration of fluids in the host rocks might have occurred by infiltration along major structures, represented by tectonised stratigraphic contacts at San Pietro and mutually cross-cutting faults at Sinibidraxiu. The sub-vertical dip of these structures had a crucial role in controlling the extent of metasomatic processes and determining the steep shape of the ore-bodies. Thus, although limited to 1–5 m thickness, they are most probably characterised by a depth-controlled zonation regulated by the fluid flow (Meinert *et al.*, 2005). These features are, in general terms, comparable to vein–skarn types (Meinert *et al.*, 2005).

For the San Pietro orebody, field and analytical evidence display a marked zonation pattern from hornfelses to marbles within a garnet–clinopyroxene–wollastonite zone. In contrast, such a prograde mineralogy and zonation has not been observed at Sinibidraxiu, where only marbles can be recognised at the contact with the orebody. However, textural evidence from the carbonates and quartz gangue such as the very fine grain size and intimate association of unusual fibrous textures, suggest replacement of pre-existing radiating aggregates of possible Ca and/or Ca–Mg silicate precursor(s) such as wollastonite and/or diopside–tremolite. In both localities, the circulation of hydrothermal fluids produced the substitution of early calc-silicate assemblages in favour of newly formed hydrous calc-silicates at San Pietro and carbonates plus quartz at Sinibidraxiu. Most ore minerals appear to be part of such retrograde assemblages, essentially confirming the evolutionary trends observed by Aponte *et al.* (1988) for other skarn occurrences in SW Sardinia. The complex variations in skarn mineralogy and composition recognised by our optical microscopy, SEM-EDS, EPMA and LA-ICP-MS studies provide data, which allow us to outline below possible evolutionary paths for the mineralising stages in different parts of the Monte Tamara skarn system.

Scheelite trace-element composition

Scheelite compositions have been used increasingly as a method for determining the origin and the physicochemical characters of fluids and the processes of formation of the orebodies (Liu *et al.*, 2019; Yuan *et al.*, 2019, Ding *et al.*, 2018; Poulin *et al.*, 2018). Accordingly, our scheelite LA-ICP-MS data allowed us to obtain many useful indications for sources of ore-forming elements and for mineralising processes at San Pietro and

Sinibidraxiu. The scheelite display seagull-wing-shaped REE chondrite-normalised distribution patterns (Fig. 17d), indicative of a magmatic source of fluids (Poulin *et al.*, 2018). As compared to those reported in literature for GS1 granites (Naitza *et al.*, 2017), chondrite-normalised REE contents are slightly to moderately lower at San Pietro and remarkably higher at Sinibidraxiu. Both scheelites display similar convex REE distribution patterns, as opposed to the concave patterns of GS1 granites. These differences may be indicative of REE fractionation under the prevailing hydrothermal conditions, arguably corresponding to greisenisation processes following granite emplacement. Hence, comparing the patterns of scheelite and the greisenised facies of the GS1 could provide clearer indications as to their genetic relationships (Poulin *et al.*, 2018). The magmatic source is also confirmed by the Sr *vs*. Eu/Eu* diagram (Fig. 17c; Poulin *et al.*, 2018) in which both scheelites lie in the magmatic field (San Pietro) or very close to it (Sinibidraxiu). The trace-element composition of scheelite, specifically REE contents and proportions, also provided useful qualitative indications about the ore forming processes. Scheelite from both orebodies have very low HREE contents with respect to LREE and middle REE (MREE) (Fig. 17f; Song *et al.*, 2014; Yuan *et al.*, 2019). However, the same diagram shows that scheelite from San Pietro are relatively enriched in LREE; a feature more distinctive of scheelite from W porphyry and W–Mo skarn deposits. In contrast, the relatively higher MREE of Sinibidraxiu scheelite are associated more usually with W vein deposits. A further indication of different mineralisation environments is provided by trends in the Ho *vs*. Y diagram (Fig. 17b; Ding *et al.*, 2018) and the REE$_{tot}$ *vs*. LREE/HREE (Fig. 17e; Ding *et al.*, 2018) diagrams. In these diagrams, San Pietro scheelite plots in or close to the W–Mo skarn field, whereas Sinibidraxiu scheelite falls very close to the granitoid field and within the W–Au hydrothermal veins field. Within a single skarn system model for the Monte Tamara area, data plotted in these diagrams might indicate a continuum from proximal W–Mo skarn deposits (San Pietro) to more distal W hydrothermal vein deposits (Sinibidraxiu). Sinibidraxiu scheelite have REE contents one order of magnitude higher than those of San Pietro scheelite. As REE substitute for Ca^{2+}, such enrichment indicates that at the stage of formation, scheelite was the most effective REE 'scavenger' in the mineral assemblage of the orebody, in agreement with the absence of other potential REE-bearing minerals such as epidote, garnet or fluorite. Although crystallised in different environments, scheelite from San Pietro and from Sinibidraxiu share similar Eu/Eu*<1 ratios (Fig. 17a–c), whereas relative Mo enrichments observed at San Pietro indicate formation under oxidising conditions (Poulin *et al.*, 2018). In fact, Mo^{6+} substitutes commonly for W^{6+} in oxidised environments, whereas Mo^{4+} precipitates readily as molybdenite under reducing conditions and in the presence of S. Arsenic is another common trace element whose presence in scheelite depends strongly on redox conditions. As-bearing scheelite are also generally formed in oxidising conditions due to As^{5+} substitutions for W^{6+}. In contrast under reducing conditions, As is not incorporated in the scheelite lattice due to the difference in ionic radii between W^{6+} and As^{2+} or As^{3+} (Poulin *et al.*, 2018). In the case of Monte Tamara, As is enriched only in San Pietro scheelite (from 2.4 to 8.2 ppm As) and is generally below the detection limit (locally up to 1.8 ppm) in Sinibidraxiu scheelite. Therefore, the As–Mo contents and the Eu/Eu*<1 ratios at San Pietro clearly record oxidising conditions. In contrast, despite the Eu/Eu*<1 ratios, the low Mo and As contents in Sinibidraxiu scheelite, together with the widespread occurrence of arsenopyrite, strongly suggest a formation under at least moderately reducing conditions.

Temperatures of formation

Temperature changes are one of the main controlling parameters in skarn formation. As a general feature, skarns are the result of fluid–rock interactions evolving from a prograde stage of temperature increase to a retrograde stage of decreasing temperature. The retrograde/sulfide stage of mineralisation corresponds to the peak of activity of hydrothermal fluids that produce hydrous minerals as overgrowths on prograde mineral associations and may precipitate sulfides and other ore minerals. To assess the temperature of the retrograde/sulfide stage in Monte Tamara skarns, the arsenopyrite, stannite and chlorite geothermometers were applied. The arsenopyrite thermometer (Kretschmar and Scott, 1976; Sharp et al., 1985) has been used for San Pietro and Sinibidraxiu arsenopyrite–pyrrhotite–pyrite mineral assemblages (Fig. 18a), Arsenopyrite coexisting with pyrrhotite (then altered to pyrite) in the San Pietro ore has an As content in the range 33.2–33.9 at.%, corresponding to a temperature range of 460–425°C. These temperatures are slightly higher than those reported for skarn retrograde stages worldwide (Meinert et al., 2005) and suggest the early formation of arsenopyrite at the boundary between prograde and retrograde stages. At Sinibidraxiu, lower temperatures have been obtained with respect to those of San Pietro, in fact, the As contents in Sinibidraxiu arsenopyrite are within the 32.3–33.1 at.% range, corresponding to temperatures of 400–375°C. The range of temperatures of the sulfide stage of San Pietro was further constrained using the stannite–sphalerite geothermometer (Shimizu et al., 2008; Shimizu and Shikazono, 1985; Nekrasov et al., 1979), based on the Fe and Zn exchange between coexisting stannite and sphalerite (Fig. 18b). For its application, stannite aggregates, locally overgrowing cassiterite in the arsenopyrite–chalcopyrite-rich ore facies (zone 3b) and stannite blebs exsolved with chalcopyrite in sphalerite in the cassiterite-bearing sphalerite–magnetite-rich ore facies (zone 2)

were considered. In addition to textural features, a relationship between stannite and cassiterite in both assemblages was considered because both share detectable Te contents. The obtained values form two clusters at different temperatures (Table S11). The first group is represented by stannite blebs in sphalerite in the sphalerite–magnetite ore facies (zone 2), which are characterised by temperature ranges of 315–284°C. The second group is represented by the stannite aggregates locally rimming cassiterite in the arsenopyrite-rich ore facies (zone 3b) which provided temperatures of 270–255°C. Such a range might be compatible with the common crustiform texture of stannite in the arsenopyrite–chalcopyrite ore facies. The stannite geothermometer thus suggests that there may be two distinct generations of stannite as also indicated by the slight compositional differences between them. Moreover, the stoichiometry of chlorite from the San Pietro retrograde assemblages, characterised by Al(IV) > 1.9 and Fe/(Fe+Mg) > 0.3, allowed the application of the geothermometer proposed by Kranidiotis and MacLean (1987), according to which a temperature range of 290–315°C was obtained for late-stage hydrothermal alteration of garnet following the initial replacement by epidote + calcite. This temperature range is markedly lower than that of arsenopyrite (460–425°C) though shows a good correspondence with the stannite blebs in sphalerite (315–284°C). Thus, the different temperatures of formation for arsenopyrite and chlorite contribute to bracketing the progression and the cooling path of retrograde alteration to which the polyphase ore mineralisation at San Pietro is related.

The prograde stage at San Pietro

In skarn systems, the oscillatory zoning in garnet reflects compositional variations in mineralising fluids, due to alternating disequilibrium and steady-state processes during infiltration into
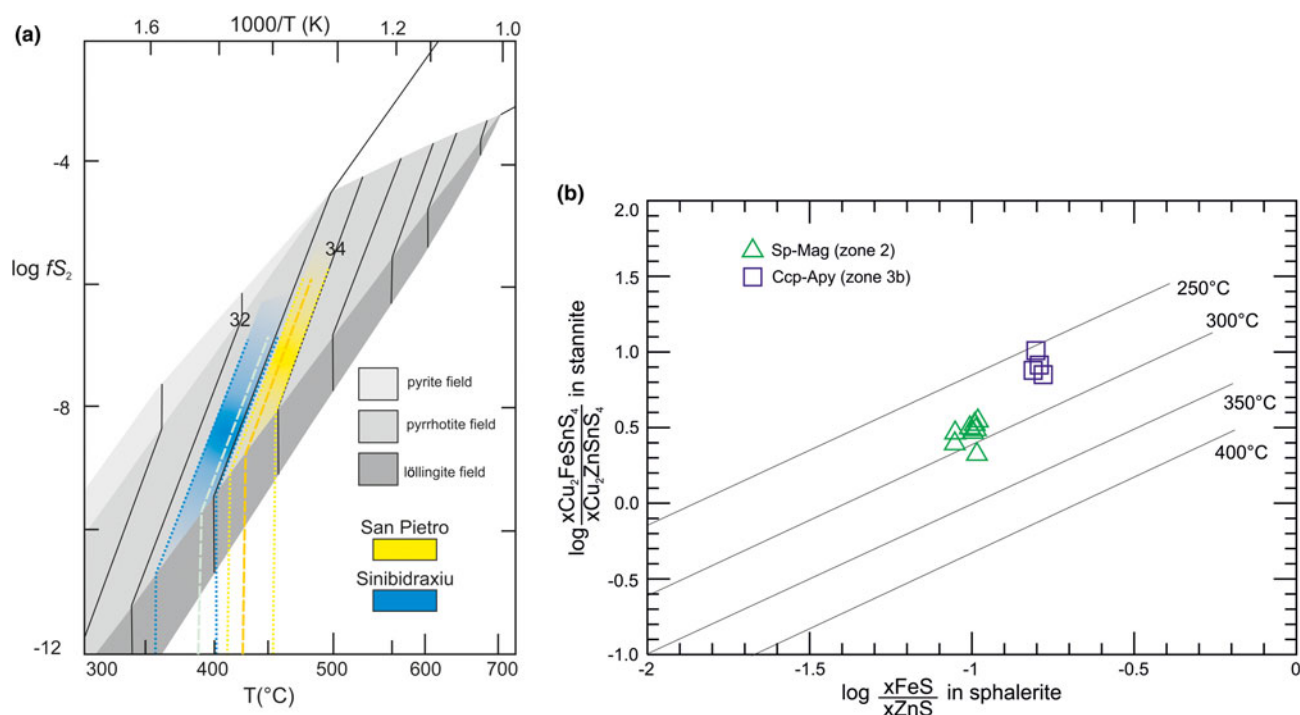

Fig. 18. Arsenopyrite (a, Sharp et al., 1985; Kretschmar and Scott, 1976) and stannite–sphalerite (b, Shimizu et al., 2008; Shimizu and Shikazono, 1985; Nekrasov et al., 1979) geothermometers and calculations of the temperatures of the retrograde/sulfide stages at San Pietro and Sinibidraxiu (a) and San Pietro (b).

the wall rocks (Park et al., 2017, 2019; Zhu et al., 2021). Abundant oscillatory-zoned grossular and andradite garnet are characteristic of the prograde-stage mineral association of San Pietro skarn. Microprobe data confirmed that: (1) in grossular, zoning corresponded to slight core/rim and rim/rim Al_2O_3 and Fe_2O_3 variations, overall leading to andradite-rich (Fe^{3+} rich) compositions; (2) both andradite and grossular garnet are variably enriched in Sn (0.4 wt.% SnO_2 on average, with maxima over 1 wt.%); and (3) Sn enrichments tend to characterise the mid to marginal portions of the zoned crystals. Overall, these features suggest precipitation from an oxidising fluid, characterised by increasing Fe^{3+} activity. In SW Sardinia, a similar trend of late Fe enrichment in the prograde stage is reported for skarns in the San Leone mine area, Eastern Sulcis (Verkaeren and Bartholomè, 1979), also related to the GS1 suite granites (Naitza et al., 2017). In the San Pietro skarn, under oxidising conditions and temperatures > 460°C (arsenopyrite geothermometer), Sn contents in garnet also increased progressively due to Sn^{4+} incorporation in octahedral sites in substitution of Fe^{3+} (Eadington and Kinealy, 1983; Galuskina et al., 2010). Sporadic W peaks recorded in garnet in the San Pietro skarn might result from W^{6+} competing with REE in the garnet lattices (Zhu et al., 2021). Diopside exhibits lower, although equally remarkable Sn contents (commonly 0.1 wt.% SnO_2, with maxima at 0.36 wt.%). Similarly to other W and W–Sn skarn deposits worldwide, in San Pietro the crystallisation of scheelite appears to correspond to the waning stage of prograde skarn (Kwak and Tan, 1981; Zaw and Singoyi, 2000; Zhu et al., 2021). Both Mo-bearing scheelite (Kwak, 1987; Zaw and Singoyi, 2000) and hematite (further pseudomorphed by magnetite) confirm the early oxidising nature of mineralising fluids in this stage. Moreover, the fine-grained fluorite interstitial to unaltered clinopyroxene suggest that F^- was present in the fluids during the prograde stage. This characteristic could relate to greisenisation processes in the more proximal, and unexposed, parts of the skarn system, which may have been of critical importance in conveying new contributions of metals from the consolidating granite outwards (Meinert, 1997).

The hydrothermal/sulfide stage at San Pietro

Both San Pietro and Sinibidraxiu skarns display abundant evidence of intense, locally pervasive retrogression of the prograde assemblages, thereby testifying a continuous intake of magmatic fluids from the consolidating granites. The growth of the coarse-grained prograde minerals enhanced the porosity of the skarns, improving the circulation of these fluids. Simultaneously, extensive alteration might have been favoured by the increase of reactive surfaces. In the San Pietro orebody, multiple pulses of fluids resulted initially in diffuse formation, at decreasing temperatures, of hydrous silicates, dominated by amphibole, epidote and chlorite, at the expense of clinopyroxene and garnet. The hydrothermal alteration of primary skarn minerals is also related to abundant precipitation of magnetite. which may indicate definite physicochemical changes in mineralising solutions, most notably variations of the redox conditions. The formation of magnetite, e.g. by substitution of early hematite (mushketovite), represents a change towards relatively more reducing conditions, below the Hematite–Magnetite buffer. The newly formed retrograde silicates partially-inherited the Sn signature of prograde silicates. This is best exemplified by epidote, whose SnO_2 contents are commonly > 0.1 wt.%. Tin might have been available for structural

substitutions in silicates (e.g. $Sn^{4+} + Ti^{4+} \rightarrow Al^{3+} + Fe^{3+}$, also with Fe^{2+} incorporation, in clinozoisite: Ordosch et al., 2019), until the establishment of favourable physicochemical conditions for cassiterite (nearly simultaneous with magnetite) and, subsequently, stannite precipitation. Notably, a source of Sn derived from the alteration of the garnet–clinopyroxene skarn, is also testified by diffuse, fine-grained cassiterite, together with scheelite, along corroded garnet rims. The concurrent sulfur increase in fluids during retrogression stabilised different sulfide assemblages. The first to form are pyrite-free sulfide assemblages, and include arsenopyrite, chalcopyrite, sphalerite, pyrrhotite, galena and Bi sulfosalts, locally surrounded by peculiar molybdenite ring-shaped aggregates. They correspond to a lower sulfur fugacity and higher temperature (arsenopyrite at 460–425°C; Fig. 18a) and are coprecipitated with accessory cassiterite. Sphalerite is ubiquitous although dominant in the magnetite-rich and in the final, pyrite-rich ore facies. The composition of sphalerite is highly variable in terms of Fe content, probably due to internal zoning of grains, reflecting fluctuations in the hydrothermal fluid conditions. A few irregular sphalerite aggregates in the early sulfide facies do not conform to the general Mn-rich character, typical of high-temperature sphalerite (Frenzel et al., 2016). Stannite was observed in the earlier, pyrite-free assemblages, although with two distinct textures, compositions and temperature ranges. As stated above, the stannite geothermometer (Fig. 18b) indicates that two distinct generations of stannite might have formed at different temperatures. The higher temperature range (315–284°C) is representative of stannite exsolved with chalcopyrite blebs in the sphalerite–magnetite-rich ore, and sporadic inclusions of cassiterite crystals are enclosed in chalcopyrite of this assemblage. The lower temperature range (270–255°C) corresponds to crustiform stannite overgrowing corroded remnants of cassiterite in the arsenopyrite–chalcopyrite ore facies. As further evidence of late-stage alteration, early pyrrhotite is locally altered to spongy pyrite–marcasite. Distribution, textures and preliminary compositional data for cassiterite (Fig. 16) suggest a protracted time span of crystallisation during the hydrothermal stage, as suggested by the rather high Fe contents (Lerouge et al., 2017).

Mineralisation at Sinibidraxiu

Compared to the San Pietro skarn, a distinct feature of the Sinibidraxiu orebody resides in the different prograde effects represented by only marble formation in the host rock. However, the gangue of the orebody is essentially composed of microscopic intergrowths dolomite–calcite and quartz, arranged as fibrous textures or irregular aggregates visible on outcrops. These might suggest hydrothermal substitution of pre-existing aggregates by the dolomite–calcite–quartz assemblage. In this case, fibrous silicates (e.g. wollastonite, diopside or tremolite) could have formed under higher temperatures than those of the early hydrothermal stage (arsenopyrite, 400–375°C). Thus, the hypothetical stages of formation of the Sinibidraxiu vein could be: (1) a first stage of formation of Ca and/or Ca–Mg fibrous silicates at temperatures ~550–400°C (Bucher and Grapes, 2011); (2) a hydrothermal stage, characterised initially by a widespread pseudomorphic substitution of fibrous silicates by dolomite–quartz and calcite roughly simultaneous with, or slightly preceding, the precipitation of arsenopyrite and sphalerite at temperatures of 400–375°C. This evolution is also indicated by the carbonate–quartz substitution of fibre-shaped inclusions in arsenopyrite and sphalerite, and by the peculiar low-Fe zones of Fe-rich sphalerite,

resembling reaction rims with such carbonate–quartz inclusions (Fig. 7g–i). Chalcopyrite aggregates are then formed, followed by galena, pyrrhotite and pyrite. Therefore, considering the lower temperature value obtained from arsenopyrite (Fig. 18) the Cu–Pb–Fe sulfides assemblage should have formed at temperatures <375°C. As discussed above, scheelite might have formed under at least moderately reducing conditions. The overall reducing character of the fluid is represented by the abundant arsenopyrite and Zn–Pb–Cu–Fe sulfides assemblage throughout the orebody and from the low As and Mo contents of scheelite.

The limited ore mineral association at Sinibidraxiu (scheelite–arsenopyrite–sphalerite, chalcopyrite, galena, pyrrhotite and pyrite) could result from a hydrothermal fluid with different characteristics to the fluid that formed the San Pietro ore. In fact, the Sinibidraxiu mineralising fluid was able to mobilise tungsten and LREE–MREE, but not Sn–Bi–Mo. The W and Sn decoupling has been observed in many W–Sn–Mo hydrothermal systems (Li et al., 2021), including in those of SW Sardinia (e.g. Monte Linas district: Deidda et al., 2021; Naitza et al., 2017). As a result, tungsten minerals (e.g. wolframite) are rarely associated with cassiterite within the same part of the orebody (Liu et al., 2021), being instead associated more commonly with molybdenite and Bi phases.

In the case of Sinibidraxiu, the absence of Sn–Bi–Mo minerals can be explained with a possible precipitation of cassiterite, molybdenite and Bi-bearing phases at greater depths in a skarn ore with similar features and evolutive paths to the San Pietro orebody. However, the distribution of W–Sn–Mo–Bi in the orebody may have been also controlled by intricate variations of many physiochemical parameters in the mineralising fluids such as chlorinity, f_{O_2} and availability of OH⁻ complexes in the fluid (Liu et al., 2021; Zajacz, 2008), all of which could be further affected by the increase of the fluid–rock reaction rate as the skarn alteration front progresses over time.

Conclusions

This investigation provided the first detailed characterisation of the mineral assemblages, paragenetic sequences and mineral composition of scheelite-bearing skarns in Sardinia. On the basis of observations and data the following conclusions can be drawn.

Mineralisation of the Monte Tamara area can be classified as oxidised (Meinert et al., 2005), W-bearing vein skarns with localised zones of enrichment of cassiterite, Bi sulfides and sulfosalts, and molybdenite.

The location and geometries of the skarn orebodies of the area are controlled strongly by the structural setting. This is exemplified by the elongated, lens-shaped and sub-vertical vein skarns along the tectonised stratigraphic contact between marbles and sandstones at San Pietro and by the sub-vertical chimney along mutually crossing faults in marbles at Sinibidraxiu.

Both orebodies record a multistage evolution, marked by mineral assemblages formed under hypo- to mesothermal conditions. At San Pietro, the prograde stage developed at temperatures of >460°C, then decreased progressively from 460–435°C (arsenopyrite), to 315–284°C (stannite inclusions in sphalerite), 315–290°C (chlorite alteration of garnet) and 270–255°C (stannite aggregates corroding cassiterite) during the retrograde/sulfide stage. The thermal evolution of the Sinibidraxiu orebody is less defined, however temperatures of >400°C can be inferred to the alleged Ca and/or Ca–Mg silicates initial stage, followed by arsenopyrite (–scheelite–sphalerite and dolomite–quartz alteration) at 400–375°C and base metal sulfides at <375°C.

The physicochemical conditions in the fluid changed progressively over time. At San Pietro, the general behaviour of redox-sensitive elements (e.g. $Fe^{3+} \rightarrow Fe^{2+}$ and $Mo^{6+} \rightarrow Mo^{2+}$) in the ore minerals records initial oxidising conditions (e.g. hematite crystallisation, andradite, lack of hedenbergite) during the prograde stage. The early As- and Mo-bearing scheelite with Eu/Eu*<1, associated with magnetite, suggests a gradual transition from mildly oxidising to progressively reducing conditions coupled with an increase in sulfur fugacity, resulting in deposition of molybdenite and base-metal sulfides. The Sinibidraxiu orebody records moderately reducing initial conditions, indicated by scheelite with low As and Mo, though with Eu/Eu*<1, evolving towards reducing conditions during arsenopyrite and base-metal sulfides formation.

The orebodies clearly show their magmatic affinity (Fig. 17). However, they are representative of different local geological controls of formation, mostly regulated by the distance from the source intrusion, within the same larger-scale W–Sn skarn system. The San Pietro orebody (Fig. 19a) and its mineralogical and compositional features suggest formation at more proximal environments very similar to other skarns worldwide (e.g. lower MREE in scheelite; presence of magnetite–cassiterite–molybdenite and Bi phases; garnet–clinopyroxene–wollastonite gangue, etc.).
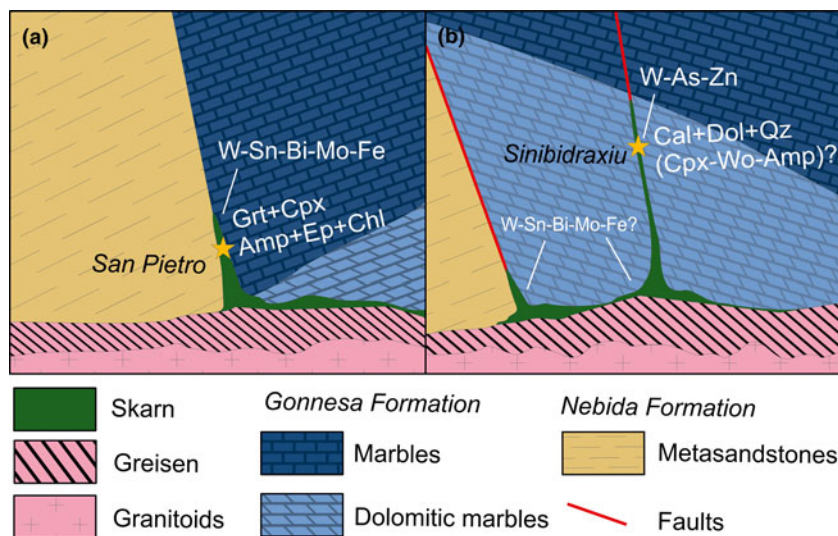

Fig. 19. Hypothetical representation of the different depth-regulated zones of the Monte Tamara skarn mineralisation system with respect to the alleged parental GS1 granites, emplaced at <2 kbar: (a) the San Pietro orebody represents a more proximal ore, including phases such as scheelite, cassiterite, molybdenite and Bi-bearing sulfosalts in a clinopyroxene-garnet skarn; and (b) the Sinibidraxiu ore has hydrothermal characters attributable to more distal environments, as suggested by the absence of molybdenite, cassiterite and Bi-bearing sulfosalts, probably deposited in deeper-seated skarns, similarly to San Pietro.

In contrast, the Sinibidraxiu orebody ([Fig. 19b](#)) is seemingly more closely related to a hydrothermal-vein environment distal to the intrusion (e.g. high MREE proportions in scheelite; absence of cassiterite–molybdenite and Bi phases; strong hydrothermal dolomite–quartz pseudomorphic substitution of fibrous silicates).

As a final consideration, the overall characteristics of both orebodies provided important guides for W, Sn and other critical raw material mineral exploration in the numerous, analogous occurrences across SW Sardinia. Moreover, this investigation supports the possibility of undiscovered mineralised outcrops and deeper-seated bodies of economic interest, particularly for W, in the whole area surrounding Monte Tamara. From a geological standpoint, this hypothesis is further supported by the structural setting of the orebodies as: (1) fault systems had a crucial role in favouring the circulation of metasomatic and ore mineralising fluids, even at large distances and along channel ways scattered along marbles; (2) the Variscan thrust-faults might have produced important 'permeability limits' at depth (e.g. due to tectonic repetitions) therefore potentially increasing the reaction rate between fluids and the carbonate host rocks; and (3) the large antiformal–synformal structure may have acted as a large trap, similar to some relevant W-skarn mineral deposits worldwide (e.g. the E orebody in the Cantung deposit: Mathieson and Clark, [1984](#); Rasmussen *et al.*, [2011](#)).

References

Aponte F, Balassone G., Boni M., Costamagna L. and Di Maio G. (1988) Variscan Skarn Ores in South-West Sardinia: their relationships with Cambro-Ordovician stratabound deposits. *Rendicondi della Società Italiana di Mineralogia e Petrologia*, **43**, 445–462.

Arthaud F. (1963) Un exemple de tectoniques superposées dans le Paleozoique de l'Iglesiente (Sardaigne). *Comptes Rendus de la Societe Géologique de France*, **9**, 303–304.

Barca S., Serri R., Rizzo R., Forci A., Calzia P. and Pertusati P.C. (2009) *Foglio 565 CAPOTERRA*. Note Illustrative della Carta Geologica d'Italia alla scala 1:50.000, Servizio Geologico d' Italia, Rome.

Barton P.B. and Bethke P.M. (1987) Chalcopyrite disease in sphalerite: Pathology and epidemiology. *American Mineralogist*, **72**, 451–467.

Boni M., Iannace A. and Balassone G. (1996) Base metal ores in the lower Palaeozoic of South-Western Sardinia. *Society of Economic Geologists, Economic Geology 75th Anniversary Volume*, **4**, 18–28.

Boni M., Stein H.J., Zimmerman A. and Villa, I.M. (2003) Re-Os age for molybdenite from SW Sardinia (Italy): a comparison with 40Ar/39Ar dating of Variscan granitoids. Pp. 247–250 in: *Mineral Exploration and Sustainable Development*. Proceedings 7th Biennial SGA Meeting, Athens, Greece.

Brizzi G.C., Scanu S., Stara P. and Tanca G. (1992a) I minerali del giacimento di Monte Tamara (Nuxis) – I° parte. *Rivista Mineralogica Italiana*, **3**, 167–180.

Brizzi G.C., Scanu S., Stara P. and Tanca G. (1992b) I minerali del giacimento di Monte Tamara (Nuxis) – II° parte. *Rivista Mineralogica Italiana*, **4**, 237–248.

Bucher K. and Grapes R. (2011) Metamorphism of dolomites and limestones. Pp: 225–255 in: *Petrogenesis of Metamorphic Rocks* (Bucher K. and Grapes R., editors). Springer, Berlin.

Burisch M., Gerdes A., Meinert L.D., Albert R., Seifert T. and Gutzmer J. (2019) The essence of time – fertile skarn formation in the Variscan Orogenic Belt. *Earth and Planetary Sciences Letters*, **519**, 165–170.

Chang Z., Shu Q. and Meinert L.D. (2019) Skarn Deposits of China. *SEG Special Publications*, **22**, 189–234.

Ciobanu C.L. and Cook N. (2000) Intergrowths of bismuth sulphosalts from the Ocna de Fier Fe-skarn deposit, Banat, Southwest Romania. *European Journal of Mineralogy*, **12**, 899–917.

Cocco F., Oggiano G., Funedda A., Loi A. and Casini L. (2018) Stratigraphic, magmatic and structural features of Ordovician tectonics in Sardinia (Italy): a review. *Journal of Iberian Geology*, **44**, 619–639.

Cocco F., Attardi A., Deidda M.L., Fancello D., Funedda A. and Naitza S. (2022a) Passive structural control on skarn mineralization localization: A case study from the Variscan Rosas Shear Zone (SW Sardinia, Italy). *Minerals*, **12**, 272.

Cocco F., Loi A., Funedda A., Casini L., Ghienne J-F, Pillola G.L., Vidal M., Meloni M.A. and Oggiano G. (2022b) Ordovician tectonics of the South European Variscan realm: new insights from Sardinia. *International Journal of Earth Sciences.*, https://doi.org/10.1007/s00531-022-02250-w

Cocozza T. (1979) The Cambrian of Sardinia. *Memorie della Società Geologica Italiana*, **20**, 163–187.

Conte A.M., Cuccuru S., D'Antonio M., Naitza S., Oggiano G., Secchi F., Casini L. and Cifelli F. (2017) The post-collisional late Variscan ferroan granites of southern Sardinia (Italy): Inferences for inhomogeneity of lower crust. *Lithos*, **294–295**, 263–282.

Damian G., Ciobanu C.L., Cook N.J. and Damian F. (2008) Bismuth sulphosalts from the galena-matildite series in the Cremencea vein, Șuior, Baia Mare district, Romania. *Neues Jahrbuch für Mineralogie – Abhandlungen*, **185**, 199–213.

Ding T., Ma D., Lu J. and Zhang R. (2018) Garnet and scheelite as indicators of multi-stage tungsten mineralization in the Huangshaping deposit, southern Hunan province, China. *Ore Geology Reviews*, **94**, 193–211.

Eadington, P.J. and Kinealy, K. (1983) Some aspects of the hydrothermal reactions of tin during skarn formation. *Journal of the Geological Society of Australia*, **30**, 461–471.

Einaudi M.T., Meinert L.D. and Newberry R.J. (1981) Skarn deposits. *Society of Economic Geologists, Economic Geology 75th Anniversary Volume*, **1981**, 317–391.

Frenzel M., Hirsch T. and Gutzmer J. (2016) Gallium, germanium, indium, and other trace and minor elements in sphalerite as a function of deposit type – a meta-analysis. *Ore Geology Reviews*, **76**, 52–78.

Funedda A. (2009) Foreland- and hinterland-verging structures in fold-and-thrust belt: An example from the Variscan foreland of Sardinia. *International Journal of Earth Sciences*, **98**, 1625–1642.

Galuskina I., Galuskin E.V., Dzierżanowski P., Gazeev V.M., Prusik K., Pertsev N.N., Winiarski A., Zadov A.E. and Wrzalik R (2010) Toturite $Ca_3Sn_2Fe_2SiO_{12}$ – a new mineral species of the garnet group. *American Mineralogist*, **95**, 1305–1211.

George L., Cook N.J., Ciobanu C.L. and Wade B.P. (2015) Trace and minor elements in galena: A reconnaissance LA-ICP-MS study. *American Mineralogist*, **100**, 548–569.

Griffin W.L., Powell W.J., Pearson N.J. and O'Reilly S.Y. (2008) GLITTER: data reduction software for laser ablation ICP-MS. Pp. 204–207 in: *Laser Ablation-ICP-MS in the Earth Sciences*. Mineralogical Association of Canada short course series, 40.

Hawthorne F.C., Oberti R., Harlow G.E., Maresch W.V., Martin R.F., Schumacher J.C. and Welch M.D. (2012) Nomenclature of the amphibole supergroup. *American Mineralogist*, **97**, 2031–2048.

Ishihara S. (1981) The granitoid series and mineralization. *Society of Economic Geologists, Economic Geology 75th Anniversary Volume*, **1981**, 458–484.

Ivashchenko V.I. (2021) Rare-Metal (In, Bi, Te, Se, Be) Mineralization of Skarn Ores in the Pitkäranta Mining District, Ladoga Karelia, Russia. *Minerals*, **11**, 124.

Kranidiotis, P. and MacLean, W.H. (1987) Systematics of chlorite alteration at the Phelps Dodge massive sulfide deposit, Matagami, Quebec. *Economic Geology*, **82**, 1898–1911.

Kretchmar U. and Scott S.D. (1976) Phase relations involving arsenopyrite in the system Fe-As-S and their application. *The Canadian Mineralogist*, **14**, 364–386.

Kwak T.A.P. (1987) *W-Sn Skarn Deposits and Related Metamorphic Skarns and Granitoids*. Developments in Economic Geology, *24*, Elsevier, pp. 451.

Kwak T.A.P. and Tan T.H. (1981) The geochemistry of zoning in skarn minerals at the King Island (Dolphin) Mine. *Economic Geology*, **76**, 468–497.

Leake B.E., Woolley R.A., Birch D.W., Burke J.A.E., Ferraris G., Grice D.J., Hawthorne C.F., Kisch J.H., Krivovichev G.V., Schumacher C.J., Stephenson C.N. and Whittaker W.J.E. (2003) Nomenclature of amphiboles: additions and revisions to the international Mineralogical Association's 1997 recommendations. *The Canadian Mineralogist*, **41**, 1355–1362.

Leone F., Hamman W., Laske R., Serpagli E., and Villas E. (1991) Lithostratigraphic units and biostratigraphy of the post-sardic Ordovician sequence in south-west Sardinia. *Bollettino della Società Paleontologica Italiana*, **30**, 201–235.

Lerouge C., Gloaguen E., Wille G. and Bailly L. (2017) Distribution of In and other rare metals in cassiterite and associated minerals in Sn±W ore deposits of the western Variscan Belt, *European Journal of Mineralogy*, **29**, 739–753.

Liu B., Li H., Wu Q.H., Evans N.J., Cai J.Y, Jiang J.B. and Wu J.H. (2019) Fluid evolution of Triassic and Jurassic mineralization in the Xitian ore field, South China: Constraints from scheelite geochemistry and microthermometry. *Lithos*, 1–15, 330–331.

Liu X., Whang W. and Zhang D. (2021) The mechanisms forming the five-floor zonation of quartz veins: a case study in the Piaotang tungsten-tin deposit, Southern China. *Minerals*, **11**, 883.

Lockington J.A., Cook N.J. and Ciobanu C.L. (2014) Trace and minor elements in sphalerite from metamorphosed sulphide deposits. *Mineralogy and Petrology*, **108**, 873–890.

Mathieson G.A. and Clark A.H. (1984) The Cantung E zone scheelite orebody, Tungsten, Northwest Territories: A revised genetic model. *Economic Geology*, **79**, 883–901.

Meinert L.D. (1995) Compositional variation of igneous rocks associated with skarn deposits – Chemical evidence for a genetic connection between petrogenesis and mineralisation, in Magmas. Pp. 401–408 in: *Fluids, and Ore deposits* (J F H Thompson, editor). Mineralogical Association of Canada Short Course series **23**. Mineralogical Association of Canada, Québec.

Meinert L.D. (1997) Application of skarn deposit zonation models to mineral exploration. *Exploration and Mining Geology*, **6**, 185–208.

Meinert L.D., Dipple G.M. and Nicolescu S. (2005) World Skarn Deposits. *Society of Economic Geologists, Economic Geology* 100*th Anniversary Volume*, **2005**, 299–336.

Moelo Y., Makovicky E., Mozgova N.N., Jambor J.L., Cook N., Pring A., Paar W., Nickel E.H., Graeser S., Karup-Møller S., Balic-Žunic T., Mumme W.G., Vurro F., Topa D., Bindi L., Bente K. and Shimizu M. (2008) Sulfosalts systematics: a review. Report of the IMA Commission on Ore Mineralogy. *European Journal of Mineralogy*, **20**, 7–46.

Naitza S., Oggiano G., Casini L., Cuccuru S., Funedda A., Secchi G. and Tocco S. (2015) Structural and magmatic controls on late Variscan metallogenesis: evidences from Southern Sardinia (Italy). Pp. 161–164 in: *Source, Transport and Metal deposits*. Proceedings of 13th Biennial SGA Meeting, Nancy, France, Vol. **1**.

Naitza S., Conte A.M., Cuccuru S., Oggiano G., Secchi F. and Tecce F. (2017) A Late Variscan tin province associated to the ilmenite-series granites of the Sardinian Batholith (Italy): The Sn and Mo mineralisation around the Monte Linas ferroan granite. *Ore Geology Reviews*, **80**, 1259–1278.

Naitza S., Fadda S., Fiori M., Peretti R. and Secchi F. (2019) The metallogenic potential of an old European mining region: the case of Sardinia (Italy). Pp. 1458–1461 in: *Life with Ore Deposits on Earth*. Proceedings of 15th Biennial SGA Meeting, Glasgow, UK, Vol. **4**.

Nekrasov I.J., Sorokin V.I. and Osadchii E.G. (1979) Fe and Zn partitioning between stannite and sphalerite and its application in geothermometry. *Physics and Chemistry of the Earth*, **11**, 739–742.

Olmi F., Sabelli C., Santucci A. and Brizzi G. (1995) Minerali rari in Sardegna. *Rivista Mineralogica Italiana*, **1**, 9–42.

Ordosch A., Raith J.G., Schmidt S. and Aupers K. (2019) Polyphase scheelite and stanniferous silicates in a W(-Sn) skarn close to Felbertal tungsten mine, Eastern Alps. *Mineralogy and Petrology*, **113**, 703–725.

Park C., Coi W., Kim H., Park. M.-H., Kang I.-M. and Lee H.-S. (2017) Oscillatory zoning in skarn garnet: Implications for tungsten ore exploration. *Ore Geology Reviews*, **89**, 1006–1018.

Park C., Park C., Song Y. and Choi S.-G. (2019) Sequential trace element analysis of zoned skarn garnet: implications for multi-stage fluxing and flow of magmatic fluid into a skarn system, *Lithos*, 350–351, 105–213.

Venerandi Pirri I. (1971) Il giacimento a blenda, galena, calcopirite di Sa Marchesa nel Sulcis (Sardegna). *Bollettino della Società Italiana di Scienze Naturali.* **62**, 505–549.

Poll J.J.K. and Zwart H.J. (1964) On the tectonics of the Sulcis area, S Sardinia. *Geologie en Mijnbouw*, **43**, 144–146.

Poulin R.S., Kontak D.J. and McDonald A. (2018) Assessing scheelite as an ore-deposit discriminator using its trace-element and REE chemistry. *The Canadian Mineralogist*, **56**, 265–302.

Rasmussen K.L., Lents D.R., Falck H. and Pattison D.R.M. (2011) Felsic magmatic phases and the role of late-stage aplitic dykes in the formation of the world-class Cantung Tungsten skarn deposit, Northwest Territories, Canada. *Ore Geology Reviews*, **41**, 75–111.

Rossi P., Oggiano G. and Cocherie A. (2009) A restored section of the "southern Variscan realm" across the Corsica-Sardinia microcontinent. *Comptes Rendus Geoscience*, **341**, 224–238.

Salvadori I. and Zuffardi P. (1961) Il giacimento di Monte Tamara. *Resoconti dell'Associazione Mineraria Sarda*, **65**(7).

Sharp D.Z., Essene E.J. and Kelly W.C. (1985) A Re-Examination of the Arsenopyrite Geothermometer: Pressure Considerations and Applications to Natural Assemblages. *The Canadian Mineralogist*, **23**, 517–534.

Shimizu M. and Shikazono N. (1985) Iron and zinc partitioning between coexisting stannite and sphalerite: a possible indicator of temperature and sulfur fugacity. *Mineralium Deposita*, **20**, 324–320.

Shimizu M., Shimizu M. and Tsunoda K. (2008) Physicochemical environment of formation of tin sulfide-bearing deposits in Japan. *Far Eastern Studies*, **7**, 23–40.

Song G., Qin K., Li G., Evans N.J. and Chen L. (2014) Scheelite elemental and isotopic signatures: Implications for the genesis of skarn type W-Mo deposits in the Chizhou Area, Anhui Province, Eastern China. *American Mineralogist*, **99**, 303–317.

Stille H. (1939) Bemerkungen betreffend die "Sardische Faltung" und den Ausdruck "ophiolitisch". *Zeitschrift Deutschen Geologischen Gesellschaft*, **91**, 771–773.

Sun S.-s. and McDonough W.F. (1989) Chemical and isotopic systematics of oceanic basalts: implications for mantle composition and processes. Pp. 313–345 in: *Magmatism in the Ocean Basins* (Saunders, A.D. and Norry, M.J., editors). Geological Society, London, Special Publications, **42**. https://doi.org/10.1144/GSL.SP.1989.042.01.19.

US Geological Survey (2021) Deposit Classification Scheme for the Critical Minerals Mapping Initiative Global Geochemical Database. *U.S. Geological Survey Open-File Report* 2021–1049, pp. 70.

Valera R. (1970) La scheelite: una nuova prospettiva nella giacimentologia sarda. *Resoconti dell'Associazione Mineraria Sarda*, **75**(8).

Valera R. and Zuffardi P. (1968) Segnalazione di Scheelite in taluni adunamenti metamorfici della Sardegna (Nota preliminare), *Resoconti dell'Associazione Mineraria Sarda*, **73**(7), 62–64.

Valera R. and Zuffardi P. (1970) La geochimica del tungsteno nel Paleozoico della Sardegna, *Rendiconti della Società Italiana di Mineralogia e Petrologia*, **26**, 815–830.

Verkaeren J. and Bartholomé P. (1979) Petrology of the San Leone Magnetite Skarn (S.W. Sardinia). *Economic Geology*, **74**, 53–66.

Voudouris P., Melfos V., Spry P.G., Bonsall T.A., Tarkian M. and Solomos Ch. (2008) Carbonate-replacement Pb-Zn-Ag±Au mineralization in the Kamariza area, Lavrion, Greece: Mineralogy and thermochemical conditions of formation. *Mineralogy and Petrology*, **94**, 85–10.

Warr L.N. (2021) IMA-CNMNC approved mineral symbols. *Mineralogical Magazine*, **85**, 291–320.

Yuan L., Chi G., Wang M., Li Z., Xu D., Deng T., Geng J. and Hu M. and Zhang L. (2019) Characteristics of REEs and trace elements in scheelite from the Zhuxi W deposit, South China: Implications for the ore-forming conditions and processes. *Ore Geology Reviews*, **109**, 585–597.

Zajacz Z., Halter W.E., Pettke T. and Guillong M. (2008) Determination of fluid/melt partition coefficients by LA-ICPMS analysis of co-existing fluid and silicate melt inclusions: Controls on element partitioning. *Geochimica et Cosmochimica Acta*, **72**, 2169–2197.

Zaw K. and Singoyi B. (2000) Formation of magnetite-scheelite skarn mineralization at Kara, Northwestern Tasmania: evidence from mineral chemistry and stable isotopes. *Economic Geology*, **95**, 1215–1230.

Zhu D.-P., Li H., Algeo T.J., Jiang W.-C. and Wang C. (2021) The prograde-to-retrograde evolution of the Huangshaping skarn deposit (Nanling Range, South China). *Mineralium Deposita*, **56**, 1087–1110.